Static Unified Inelastic Model
pre- and post-yield dislocation-mediated deformation

Van Dokkum, Jan Steven; Bos, Cornelis; Offerman, Sven Erik; Sietsma, Jilt

DOI
10.1016/j.mtla.2023.101694

Publication date
2023

Document Version
Final published version

Published in
Materialia

MTLA 27 (2023) 101694

Contents lists available at ScienceDirect

Materialia

journal homepage: www.elsevier.com/locate/mtla

Full length article

Static Unified Inelastic Model: pre- and post-yield dislocation-mediated deformation

Jan Steven Van Dokkum [a,*], Cornelis Bos [a,b], Sven Erik Offerman [a], Jilt Sietsma [a]

[a] Department of Materials Science and Engineering, Delft University of Technology, 2628 CD Delft, The Netherlands
[b] Tata Steel Research & Development, P.O. box 10000, 1970 CA IJmuiden, The Netherlands

ARTICLE INFO

Keywords:
Yield criterion
Work-Hardening modelling
Dislocation structure
Cyclic stress–strain curve
Anelasticity

ABSTRACT

Modelling dislocation glide over the initial part of a stress–strain curve of metals received little attention up to now. However, dislocation glide is essential to ones understanding of the fundamental relationship between inelastic deformation and the evolution of the dislocation network structure. Therefore, we present a model of dislocation-driven deformation under static loading conditions.

We reproduce repeated cyclic uniaxial tensile tests on Interstitial-Free and Low-Alloy steels. The elastic mechanical behaviour is described by isotropic linear elasticity, pre-yield anelastic mechanical behaviour by a dislocation bow-out model with dissipation, and the post-yield evolution of dislocation network structure by a statistical storage model. We hypothesise that when the local anelastic compliance is lower than the global plastic compliance, deformation is mechanically recoverable, and *vice versa*. This hypothesis is corroborated with the classical Taylor relation. We report the relation between stable and unstable dislocation glide using this prototypical modelling framework.

We find four structural variables, that are based on dislocation physics, to describe the stress–strain curve: total dislocation density, average dislocation segment length, dislocation junction formation rate, and average dislocation junction length. Firstly, we quantify the dislocation network evolution during uniaxial monotonic loading, and verify work-hardening by dislocation junction formation and a Taylor-type equation for flow. Finally, we present a semi-empirical relation for the evolution of the dislocation network structure. Which allows us to: refine the physical interpretation of the Taylor relationship, and rationalise experimental observations on apparent modulus degradation by thermomechanical processing. Both these findings circumvent the limitations of current, physics-based hardening models.

1. Introduction

Metals typically undergo significant deformation before they fracture. The force per unit area necessary to continue deformation increases with the previously applied plastic strain, which is called strain or work hardening. Hence hardening is commonly associated with plasticity. A lesser studied type of deformation is anelasticity, i.e. recoverable nonlinear mechanical behaviour, as observed by [1–7]. Anelastic deformation is an additional strain component on top of the elastic lattice strain during loading and unloading. Li and Wagoner [7] show that anelastic deformation is dissipative yet mechanically recoverable, while plastic deformation is both thermodynamically and mechanically irrecoverable. The physical interpretation of yield thus is the transition from mechanically recoverable to mechanically irrecoverable deformation. Both types of deformation are inelastic, that literately means non-elastic.

1.1. Background

At temperatures below about one-third of the melting point of metals, dislocation glide is the dominant mechanism of inelastic deformation [8]. It is common knowledge that the mechanical deformation of metals is chiefly governed by the generation, glide and storage of dislocations [9]. The key microstructural feature thus is the dislocation network [8,10]. The structure of the dislocation network is complex, with a distribution of dislocation-link lengths [8,11]. The network is a continuous structure that consists of dislocation links delimited by microstructural features like precipitates, solute atoms, grain boundaries, and junctions with adjacent dislocations within the same net [9,12]. Those points of interaction, which include all microstructural defects that impede local dislocation motion, are commonly known as pinning points [9]. A schematic representation of a dislocation link bound by two forest dislocations is presented in Fig. 1(a).

* Corresponding author.
E-mail address: j.s.vandokkum@tudelft.nl (J.S. Van Dokkum).

https://doi.org/10.1016/j.mtla.2023.101694
Received 28 November 2022; Accepted 22 January 2023
Available online 7 February 2023

Nomenclature

α	Proportionality (–)
α'	Taylor relationships' constant (–)
b	Burgers vector magnitude (L)
β	Junction formation rate (–)
$\bar{\beta}$	Work-hardenability (–)
C	Constant (– & L^{-1})
γ	Shear strain (–)
E	Elastic modulus ($ML^{-1}t^{-2}$)
ϵ	Strain (–)
Θ	Tangent modulus ($ML^{-1}t^{-2}$)
j & k	Slip-system indices (–)
l	Segment length (L)
L	Length
M	Taylor factor (–)
M	Mass
μ	Shear modulus ($ML^{-1}t^{-2}$)
N	Number (–)
ν	Poisson's ratio (–)
ξ	Junction length (L)
R	Radius (L)
RMSE	Root mean-square error (–, L^{-2} & $ML^{-1}t^{-2}$)
R^2	Coefficient of determination (–)
ρ	Dislocation density (L^{-2})
$\hat{q}^{-1}$	Hardening ratio (–)
S	Area (L^2)
σ	Stress ($ML^{-1}t^{-2}$)
τ	Shear stress ($ML^{-1}t^{-2}$)
t	time
V	Volume (L^3)
ϕ	Angle (–)
x & z	Cartesian coordinates (L)

The motion of a given dislocation link, which is an initially straight dislocation segment under zero Peach–Koehler force delimited by pinning points, was first described by Frank and Read, and is known as a Frank–Read source [14,15]. A schematic representation of the Frank–Read (FR) source is given in Fig. 1(b). While a given link, that is delimited by stable junctions, bows out on its glide plane and not yet attains its critical, semicircular shape, the shear strain contribution is mechanically reversible [1]. The interaction between dislocations on non-parallel planes during Stage-II hardening forms these stable junctions that are strong obstacles to local dislocation motion [16]. When a link attains its critical shape, the link starts acting as a so-called source [15]. The ensuing dislocation loop, if unimpeded, keeps expanding. The latter action is commonly referred to as the activation of Frank–Read sources, and herein, the main mechanism for dislocation density increase.

Plastic mechanical deformation is commonly captured in work-hardening models, e.g. Kocks [17], Kocks and Mecking [18], Estrin and Mecking [19], Bergström [20,21], Bergström-Van Liempt [22,23] and internal-variable models [24,25], which make use of volume averaged quantities, e.g. the total dislocation density, average storage distance and average interaction range. In the remainder of the present work, we consider static loading conditions [16], i.e. time-dependent (dislocation) interactions that take place at much shorter timescales than the rate of loading and unloading. Hardening models consist of two parts [26]. The *first* part describes the dislocation network evolution. The dislocation network structure evolves by the glide of activated dislocation links, commonly called mobile dislocations [9,16]. The global dislocation density increases and the average dislocation segment length decreases on a given (active) slip-system [26]. Upon load reversal, the stored, previously mobile, dislocation links reverse their motion. Yet, they remain inactive as Frank–Read sources because the dislocation network refined concurrently. Plastic deformation is thus uniquely defined after unloading, i.e. the area swept by mobile dislocations whilst hardening minus the mechanically recoverable anelastic component of the total strain. Virtually all present work-hardening models neglect anelastic strain; the *second* part of hardening models consists of a flow rule that relates the current dislocation network geometry to the global flow strength. Commonly the flow strength is determined by a Taylor-type equation [27]. The Taylor relation is sometimes rationalised with the force necessary to activate dislocation links [28], under the assumption that the average segment length scales with the square root of the dislocation density [8,26]. In the Taylor model, hardening is thus due to either the increase in global dislocation density [27] and/or the decrease of local dislocation segment lengths [28]. Taylor-type equations assume solely linear elastic pre-yield behaviour, although dislocations mechanics is modelled [27,29]. Hence there are few studies that explicitly model dislocation glide over the entire stress–strain curve of metals. Currently, we are solely aware of the work by Torkabadi et al. [30], who use a mixed physical-phenomenological model. More common are hyperelasticity and Mroz-like multi-surface descriptions of continuum inelasticity, and complex path- and direction-dependent hardening models of continuum plasticity (See [7] for an extensive overview).

Several yield strength models do explicitly consider dislocation motion before massive dislocation multiplication initiates. Recently, Van Liempt and Sietsma [4] postulate a yield criterion based on the identification of the transition in dislocation behaviour from limited reversible glide in the pre-yield stage, without essential changes in the dislocation structure, to post-yield dislocation multiplication. The methodology as championed by Van Liempt and Sietsma [4] yields the dislocation density and a measure of dislocation segment lengths. Li and Wagoner [7] present a dissipative dislocation bow-out model, that they [7] state reproduces anelastic unloading–reloading hysteresis. The aforementioned dislocation bow-out models [4,7] excel in capturing the dissipative and mechanically reversible pre-yield deformation, however omit significant mechanically irreversible dislocation motion, that is at the origin of plastic strain and hardening. The flow strength description in current hardening models juxtaposed to bow-out models [4–7] leads to solely linear elastic behaviour; the majority of work-hardening models lacks a description of reversible dislocation motion and bow-out models [4–7] omit significant irreversible dislocation motion. From an engineering perspective, the total recoverable strain during loading and unloading governs the apparent elastic modulus [1–3,31,32], which is essential for materials models of cyclic loading and precision engineering [4,7,33], and in spring-back and thermomechanical processing of metals alloys [5,30,34]. Especially the nonlinear unloading–reloading behaviour in thermomechanical manufacturing processes is ill understood, which directly affects the process parameters, and assurance of products' properties and quality [35]. There is thus a distinct need for a unified inelastic model, where the physics-based descriptions of the anelastic and plastic strain are combined, that currently lacks in literature.

1.2. Outline

We propose a novel yield criterion that encompasses both the local behaviour of individual sources and the global dislocation interactions that constitute hardening. First, we ensure that the bow-out model and a statistical storage [36] model share the same set of dislocation structural variables, which is the *unification* in the present work. Then, we hypothesise that when the local anelastic compliance is higher

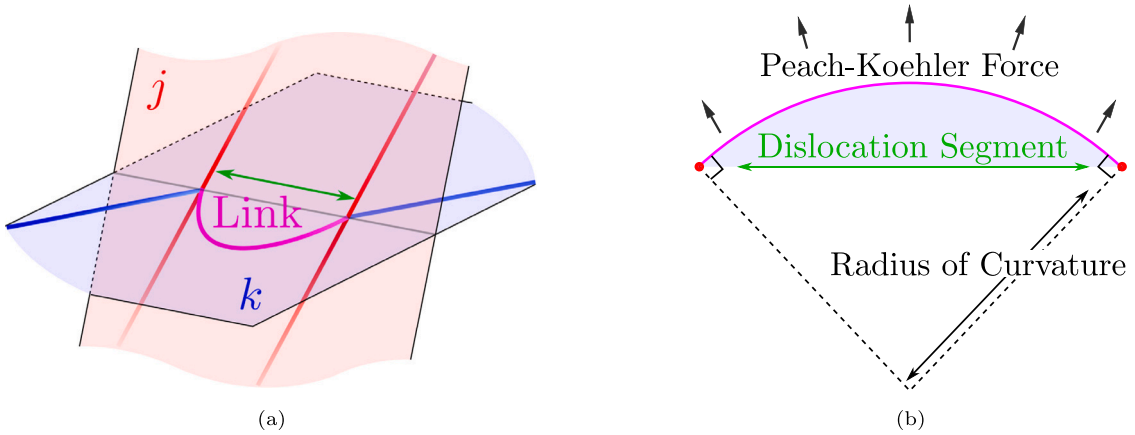

Fig. 1. Schematic representation of (a) a dislocation link on slip system k pinned by two forest dislocations on slip system j, and (b) a Frank–Read source with an initially straight dislocation segment. Adapted from [4,13], respectively.

than the global plastic compliance, deformation is mechanically irrecoverable, and *vice versa*. In this work, we construct a model of inelastic deformation under static loading conditions. The unified inelastic model consists of three parts: part *one* describes the anelastic deformation in the absence of structural change in the dislocation network, i.e. the dissipative dislocation bow-out model [7]. Here, we simplify the quasi-static bow-out model by Benzerga et al. [37]; part *two* describes the structural change of the dislocation network with plastic strain. Here, we re-interpret the proto(type)-statistical storage model by Kocks [17]; and, part *three* is the physics-based criterion that identifies the transition from mechanically recoverable to irrecoverable deformation. The present model must be: *general*, to apply to various metals; *concise*, to represent dislocation physics; *consistent*, to incorporate commonplace material properties; and, *transparent*, to uniquely capture the stress–strain curves shape. These steps allow us to define the four unique physical, structural variables of total dislocation density, average segment length, junction formation rate and average junction length. Herewith we finalise our unified model, that we use to analyse uniaxial tensile force–displacement curves.

All is performed under the following main assumption: *the proportionality α between the square root of the dislocation density $\sqrt{\rho}$ and the number of junctions per unit dislocation length $1/\langle l\rangle$ is constant for monotonic uniaxial loading in each cycle*. This is based on the relation between the aforementioned proportionality α and the Taylor relationships' constant α' [27] as proposed by Arechabaleta et al. [6]. The proportionality $\alpha \equiv 1/\left(\langle l\rangle\sqrt{\rho}\right)$ thus represents the geometry of the dislocation network, wherein the global dislocation density is connected to the local dislocation-link structure as described by average dislocation segment length $\langle l\rangle$. From a physics perspective, we identify a disparity between the invariance of the Taylor relationships' constant α' during work hardening, which is widely accepted, and the different functional forms of the proportionality α. Several works find that the proportionality α is constant [6,26,38], while others [5,7,8] report that it decreases with plastic deformation.

In the remainder, the following results are presented and discussed: *first*, we corroborate our definition of yield with the square root dependence of the yield strength on dislocation density. Wherefore we analyse the experimental force–displacement results of asymmetric stress, low cyclic, uniaxial ratcheting of single phase, Interstitial-Free and Low-Alloy, steels [5,6]. Moreover, we find our definition of yield to be in keeping with the Taylor relationship [27]; *then*, we reproduce the evolution of average dislocation segment length and density with plastic monotonic uniaxial loading. Combining these findings, we construct the statistical storage-base work-hardening model. The statistical storage-based work-hardening model allows us to verify that the Taylor relationship captures the flow stress increase with dislocation network structure evolution; *finally*, we find that the proportionality α decreases monotonically with plastic strain, yet distinctly different from previous reports [6,7]. These observations prompt us to experimentally quantify the evolution of the dislocation network structure. Hence we derive a new, semi-empirical relation of proportionality change that accompanies work hardening. This relation then allows us to: present a new physical interpretation for the Taylor relationships' constant α'; rationalise previous experimental observations [30,32,35,39–42] on the changes in initial apparent moduli with thermomechanical processing; and, finally, we propose a first step towards improving the current unified inelastic model.

With the present work, the in-depth understanding of the fundamental relationships between limited plastic deformation and the dislocation structure, and the mechanical properties of anelastic deformation, yield and flow are advanced. We contribute to current works [4–7] with a seamless, unified stress–strain treatment, that combines the three deformation mechanisms of elastic bond stretching, stable and unstable dislocation glide. The unified model allows us to ascertain the Taylor relationship and the proto-statistical storage model; two premises of physical metallurgy. *Ergo* we establish a physics-informed connection between the geometry of the dislocation network, by proportionality α, and the Taylor relationships' constant, α'.

2. Theory

For an isotropic mechanical response and uniaxial loading σ, the total principal strain is

$$\epsilon\left(\sigma\right) = \epsilon_{\mathrm{el}}\left(\sigma\right) + \epsilon_{\mathrm{in}}\left(\sigma\right) = \frac{\sigma}{E} + \epsilon_{\mathrm{an}}(\sigma) + \epsilon_{\mathrm{pl}}(\sigma), \tag{1}$$

with elastic lattice strain ϵ_{el}, inelastic strain ϵ_{in}, and anelastic and plastic strains, ϵ_{an} and ϵ_{pl}, respectively, where E is the isotropic linear elastic modulus. Here, the Roman subscript $_{\bullet}$ indicates a given mean-field property $\bullet$. In the following, we consider solely isothermal deformation conditions.

2.1. Anelastic strain

A pinned dislocation segment with length l lays along the x-axis with the applied shear stress τ^{PK} in Fig. 2. Benzerga et al. [37] solved the differential equation of motion, under quasi-static loading conditions, of a single dislocation link for a constant Peach–Koehler force $\tau^{\mathrm{PK}}b$, with the Burgers vector magnitude b. The Roman superscript * indicates a given specification $\bullet$. These quasi-static loading conditions mean that the solution of the differential equation of motion is approximated by omission of inertia [43]. Under static equilibrium, the velocity of the dislocation line vanishes and the given link's curvature is

$$\frac{1}{R} = \frac{2\tau^{\mathrm{PK}}}{\mu b}, \tag{2}$$

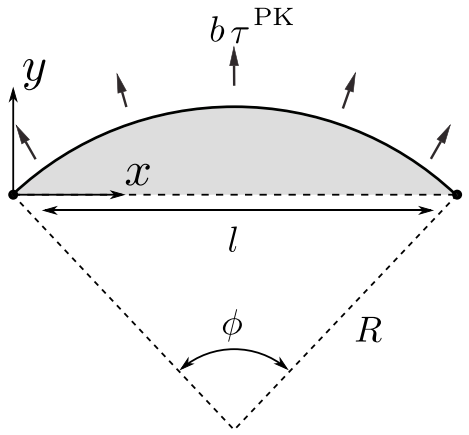

Fig. 2. Schematic representation of a dislocation link with radius of curvature R, subtended angle ϕ and swept area S indicated by a grey semicircle.
Source: Adapted from [4].

where $\mu = E/(2(1+\nu))$ is the linear elastic shear modulus, with Poisson's ratio ν. The area swept by the given link is

$$S(\phi) = \begin{cases} -\pi R^2 - \frac{1}{2}R^2(\phi - \sin(\phi)), & -\pi \geq \phi > -2\pi; \\ \frac{1}{2}R^2(\phi - \sin(\phi)), & \pi > \|\phi\| \geq 0; \\ \pi R^2 - \frac{1}{2}R^2(\phi - \sin(\phi)), & \pi \leq \phi < 2\pi; \end{cases}, \tag{3}$$

with the subtended angle

$$\phi(R/l) = \begin{cases} -2\pi - 2\sin^{-1}(l/(2R)), & R < -\frac{l}{2}; \\ 2\sin^{-1}(l/(2R)), & \|R\| \leq \frac{l}{2}; \\ 2\pi - 2\sin^{-1}(l/(2R)), & \frac{l}{2} < R; \end{cases}. \tag{4}$$

Substituting Eqs. (2) and (4) in Eq. (3), we obtain the swept area for shear stress $\tau^{\mathrm{PK}} < \mu b/l$ as

$$S\left(\tau^{\mathrm{PK}}, l\right) = \frac{l^2}{8}\left(\frac{\tau^{\mathrm{c}}}{\tau^{\mathrm{PK}}}\right)^2\left(2\sin^{-1}\left(\frac{\tau^{\mathrm{PK}}}{\tau^{\mathrm{c}}}\right) - \sin\left(2\sin^{-1}\left(\frac{\tau^{\mathrm{PK}}}{\tau^{\mathrm{c}}}\right)\right)\right), \tag{5}$$

with the critical line stress $\tau^{\mathrm{c}} \equiv \mu b/l$. In the following, pre-yield dislocation motion is limited to planar glide.

We take the local Peach–Koehler force $\tau^{\mathrm{PK}}b$ equal to $\tau_k b$, with resolved shear stress τ_k in slip system k. Note that the Italic subscript $_{\bullet}$ is not the index notation, but indicates a given slip system $_{\bullet}$. The anelastic shear strain is

$$\gamma_k^{\mathrm{an}}(\tau_k) = \frac{b\rho_k}{\langle l_k\rangle} S\left(\tau_k, \langle l_k\rangle\right), \tag{6}$$

where the average segment length $\langle l_k\rangle$ is related to the dislocation density ρ_k on slip system k. We thus consider a dislocation-link length-distribution, that we model implicitly by representative, volumetric mean, dislocation structural properties $\bullet$ indicated by $\langle\bullet\rangle$.

2.2. Statistical storage model

Kocks [17,36] constructed a self-styled statistical dislocation storage and dynamic recovery model. This early model, often called prototype [44] and/or Kocks–Mecking model, is *a posteriori* rationalised by the empirical Palm–Voce equation [45,46]. The formulation is originally based on the forest strengthening model [10,47], although this is not advocated as such in the earliest publication [17]. Furthermore, the dislocation interaction is confined to interaction between mobile and forest dislocations, and the model was formulated for zero Kelvin as well. In order to relate the flow strength at 0 K to the glide flow stress at finite temperatures and applied strain rates, one can use, following [17,44,48], a simple Arrhenius expression for thermally activated glide. We extend this proto-statistical storage-based model.

Mobile dislocation links travel a given distance till they interact with microstructural obstacles and/or (other) dislocations. The latter interaction predominantly forms stable junctions between dislocation lines on the given slip system and/or forest planes. We refer to this process as dislocation storage and gave a schematic representation thereof in Fig. 1(a). Another part of the dislocation density annihilates because oppositely signed dislocations meet, or they reach free surfaces and grain boundaries. We thus write the forest dislocation structure evolution as:

$$\frac{\partial\rho_j}{\partial\epsilon_{\mathrm{pl}}} = \frac{\partial\rho_j^+}{\partial\epsilon_{\mathrm{pl}}} - \frac{\partial\rho_j^-}{\partial\epsilon_{\mathrm{pl}}}. \tag{7}$$

The forest structure evolution describes the creation and loss of a given part of the junction density ρ_j, where slip systems j form junctions with a given slip system k. Note that the junction density ρ_j is the number of potential junction sites to be formed between a given mobile dislocation link on slip system k with the given dislocation link on system j. Here, the first term on the right-hand side of Eq. (7) is defined by the chance that a mobile dislocation encounters a potential junction and, subsequently, forms a (stable) junction. Therefore, assuming a model with the mean free path on slip system k given by the effective junction spacing $\left(\sqrt{\rho_j}\left\langle\beta_{kj}\right\rangle\right)^{-1}$, we write the storage term as:

$$\frac{\partial\rho_j^+}{\partial\epsilon_{\mathrm{pl}}} = \left\langle\beta_{kj}\right\rangle\rho_k^{\mathrm{m}}\sqrt{\rho_j}\frac{\partial\langle R_k\rangle}{\partial\epsilon_{\mathrm{pl}}}, \tag{8}$$

where $\mathrm{d}\langle R_k\rangle$ is the average distance travelled by mobile dislocation lines per unit of volume ρ_k^{m} during a principal strain increment $\mathrm{d}\epsilon_{\mathrm{pl}}$. Furthermore, the mean junction formation rate $\langle\beta_{kj}\rangle$ [49,50] is assumed to be temperature independent, and, as will be shown, an effective measure that relates the dislocations on slip system k to the dislocation densities on all slip systems, which include system k. The double Italic subscripts $\bullet_{kj}$ indicate the interaction matrix $\bullet$ of a given dislocation property of slip j on a given dislocation property of slip system k. The individual components of these interaction matrices are not determined herein, but their effective values on a polycrystalline level are in the following.

The second term on the right-hand side of the structure evolution (7) describes a recovery or a rearrangement process that occurs on junctions when impinged by mobile dislocations. The number of potential recovery sites a mobile dislocation meets during the principal strain increment $\mathrm{d}\epsilon_{\mathrm{pl}}$ is defined as:

$$\mathrm{d}N_{kj}^{\mathrm{recov}} \equiv \rho_j\left(\epsilon_{\mathrm{pl}}\right)\mathrm{d}\langle S_k\rangle, \tag{9}$$

where $\langle S_k\rangle$ is the average area swept by a mobile dislocation on slip system k. An average junction length $\left\langle\xi_{jk}\right\rangle$ of the junction density ρ_j gets recovered at each potential recovery site [17]. We thus find that the average, recovered junction length per unit of volume V is

$$\frac{\partial\rho_j^-}{\partial\epsilon_{\mathrm{pl}}} = \frac{\rho_j\left\langle\xi_{jk}\right\rangle}{V}\frac{\partial\langle S_k\rangle}{\partial\epsilon_{\mathrm{pl}}}. \tag{10}$$

Typically, one increases $\left\langle\xi_{jk}\right\rangle$ by means of a power law to describe cross-slip of screw dislocations at low to intermediate temperatures and vacancy assisted climb from intermediate up to high temperatures [44].

The assumption is made that the probability of a recovery event per unit of distance a dislocation travels is proportional to the number of times that a potential recovery site is contacted by a moving dislocation, i.e.,

$$\rho_k^{\mathrm{m}}\mathrm{d}\langle R_k\rangle \propto \mathrm{d}\langle S_k\rangle/V. \tag{11}$$

This is equivalent to the Orowan equation and therefore we write:

$$\frac{\partial\gamma_k^{\mathrm{pl}}}{\partial\epsilon_{\mathrm{pl}}} \approx b\rho_k^{\mathrm{m}}\frac{\langle R_k\rangle}{\epsilon_{\mathrm{pl}}} \approx \frac{b}{V}\frac{\partial\langle S_k\rangle}{\partial\epsilon_{\mathrm{pl}}}, \tag{12}$$

where γ_k^{pl} is the plastic shear strain on slip system k. By substituting Eqs. (8), (10) and (12) in Eq. (7) and using the chain rule, we find:

$$\frac{\partial \rho_j}{\partial \gamma_k^{\mathrm{pl}}} = \frac{\langle \beta_{kj} \rangle \sqrt{\rho_j}}{b} - \frac{\langle \xi_{jk} \rangle \rho_j}{b}. \tag{13}$$

We relate the potential junction-dislocation density to average area per junction on given slip system k, and take $\rho_j\left(\epsilon_{\mathrm{pl}}\right) \equiv \alpha_{jk}^2 \rho_k\left(\epsilon_{\mathrm{pl}}\right)$ for a dislocation net with homogeneous junction spacing, i.e. uniformly distributed junction sites characterised by the length scale $\langle l_k \rangle$. The density increase on given plane thus reads

$$\frac{\partial \rho_k}{\partial \gamma_k^{\mathrm{pl}}} = \frac{\langle \beta_{kj} \rangle \sqrt{\rho_k}}{\alpha_{jk} b} - \frac{\rho_k \langle \xi_{jk} \rangle}{b}, \tag{14}$$

where we assume that the proportionality $\alpha_{jk} \equiv \left(\sqrt{\rho_k}\langle l_k \rangle\right)^{-1}$ is constant during monotonic plastic straining in each loading cycle. This is approximately satisfied for monotonic plastic strain $\epsilon_{\mathrm{m}}^{\mathrm{pl}} \lessapprox 5 \times 10^{-3}$ as shown in the following.

Contrary to the number of potential junctions per area of slip plane ρ_j, density ρ_k is the dislocation density on slip system k. Substituting the proportionality α_{jk} into Eq. (14), the evolution of the average dislocation segment length is given by the ordinary differential equation

$$\frac{\partial \langle l_k \rangle}{\partial \gamma_k^{\mathrm{pl}}} = \frac{\langle \xi_{jk} \rangle \langle l_k \rangle}{2b} - \frac{\langle \beta_{kj} \rangle \langle l_k \rangle^2}{2b}. \tag{15}$$

When the network refinement $\mathrm{d}\langle l_k \rangle$ equals zero, we find the minimum segment length $\lim \langle l_k \rangle \left(\epsilon_{\mathrm{pl}} \to \infty\right) \sim \langle \xi_{jk} \rangle / \langle \beta_{kj} \rangle$, i.e. the scaled projection of average junction length $\langle \xi_{jk} \rangle$ is recovered at each recovery site, and the network no longer refines.

2.3. Yield strength

The definition of global, plastic flow strength before yield is ambiguous because dislocation mediated deformation is limited without the glide of activated dislocation links. However, when mobile dislocation loops are present with radii larger than the average dislocation segment length, they move at Peach–Koehler forces that are a fraction of those necessary to maintain pre-yield reversible deformation. Moreover, these dislocation loops shear across larger areas than dislocation links do at pre-yield stress. So we hypothesise that when the local anelastic compliance is lower than the global plastic compliance, deformation is mechanically recoverable. *Vice versa*, once the local anelastic compliance is higher than the global plastic compliance, inelasticity is mechanically irrecoverable. The least compliant type of deformation thus describes post-yield mechanical deformation. Compliance is the ratio of strain to stress with units of inverse stress, analogue to the inverse of the stiffness.

In Fig. 3, a schematic representation of the yield-point by shear stress-inelastic strain curves is given. At yield, we then ensure the flow curve and tangent modulus are continuous and write the criteria:

$$\Theta_k^{\mathrm{pl}}\Big|_{\tau_k=\tau_k^{\mathrm{y}}} \equiv \Theta_k^{\mathrm{an}}\Big|_{\tau_k=\tau_k^{\mathrm{y}}}; \qquad \text{and,} \qquad \lim_{\tau_k \to \left(\tau_k^{\mathrm{y}}\right)^+} \gamma_k^{\mathrm{pl}} \equiv \lim_{\tau_k \to \left(\tau_k^{\mathrm{y}}\right)^-} \gamma_k^{\mathrm{an}}, \tag{16}$$

i.e. at yield the anelastic and plastic compliance are equal. The post-yield tangent modulus thus is larger for plastic than for anelastic deformation, which is obvious from experiments [4–7]. Note that by the right-hand side of Eq. (16), the pre-yield anelastic deformation becomes plastic deformation when yield occurs, and we choose to neglect pre-yield micro-plasticity. A finite yield stress based on a Taylor-style relations considers forest dislocations [51], junction strengthening [52] and/or a combination of both [29]. A potential plastic flow rule thus is defined as:

$$\tau_k\left(\epsilon_{\mathrm{pl}}\right) \equiv \alpha_{kj} \mu b \sqrt{\rho_j(\epsilon_{\mathrm{pl}})}. \tag{17}$$

The novel yield criterion and the Taylor-type equation (17) are distinct herein.

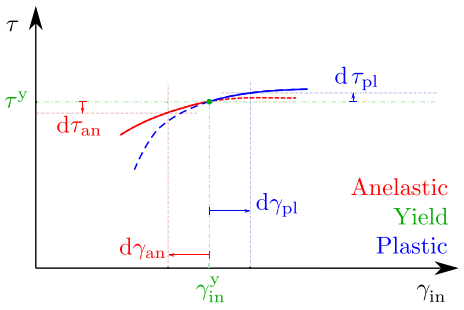

Fig. 3. Schematic representation of the novel yield criterion by shear stress-inelastic shear strain curves. (For interpretation of the references to colour in this figure legend, the reader is referred to the web version of this article.)

3. Calculation

We use the relation between the normal stress and resolved shear stress, and the principal inelastic strain and inelastic shear strain as given by the Taylor factor M. Assuming dislocation lines to be, *one*, homogeneously dispersed, and *two*, uniformly distributed over k slip-systems with dislocation density ρ_k each, i.e. the total dislocation density $\sum_k \rho_k \equiv k\langle \rho_k \rangle$, we approximate the resolved shear stress and principal inelastic strain by

$$\tau \approx \frac{\sigma}{M}, \qquad \text{and} \qquad \epsilon_{\mathrm{in}}(\sigma) \approx \frac{1}{M} \sum_k \gamma_k^{\mathrm{in}}(\tau), \tag{18}$$

respectively.

In the following, the average junction length $\langle \xi_k \rangle$, the mean junction formation rate $\langle \beta_k \rangle$ and proportionality α_k are assumed to represent dislocation statistics of $\langle \xi_{jk} \rangle$, $\langle \beta_{kj} \rangle$ and α_{jk}, respectively, which is necessary for the Taylor homogenisation. This requires the average junction length $\langle \xi_k \rangle$, the mean junction formation rate $\langle \beta_k \rangle$ and proportionality $\alpha_k = \left(\sqrt{\rho_k}\langle l_k \rangle\right)^{-1}$ to be solely properties of the given slip system k. Variable with the given Roman subscript $_k$, and several without, e.g. proportionality α_k, thus are spatially averaged values, here across grains, that represent the given, more complex polycrystalline morphology.

3.1. Flow curve

In this work, the plastic shear strain γ_k^{pl} relates to the dislocation density ρ_k via

$$\frac{\partial \rho_k}{\partial \gamma_k^{\mathrm{pl}}} = \frac{\langle \beta_k \rangle}{\alpha_k b} \sqrt{\rho_k\left(\gamma_k^{\mathrm{pl}}\right)} - \frac{\langle \xi_k \rangle}{b} \rho_k\left(\gamma_k^{\mathrm{pl}}\right). \tag{19}$$

The maximum dislocation density is $\rho_k^{\max} = \left(\alpha_k \langle \xi_k \rangle / \langle \beta_k \rangle\right)^{-2}$, which corresponds with the total density of created dislocation line being recovered. The flow strength is

$$\tau_k\left(\gamma_k^{\mathrm{pl}}\right) = \alpha_k \mu b \sqrt{\rho_k(\gamma_k^{\mathrm{pl}})} = \mu b / \langle l_k\left(\gamma_k^{\mathrm{pl}}\right) \rangle, \tag{20}$$

where the average dislocation-link length is equal to the mean potential junction spacing. The inelastic shear strain $\gamma_k^{\mathrm{in}} = \gamma_k^{\mathrm{an}} + \gamma_k^{\mathrm{pl}}$ on slip system k is derived in Appendix A. Given the anelastic and plastic tangent moduli, Eqs. (A.3) and (A.6), respectively, are symmetric, and substituting them into the left-hand side term of Eq. (16), we obtain the inverse hardening ratio

$$\hat{q}_k = \frac{1}{\dfrac{\bar{\tau}_k^{\mathrm{y}}}{\sqrt{1-\left(\bar{\tau}_k^{\mathrm{y}}\right)^2}} - \sin^{-1}\left(\bar{\tau}_k^{\mathrm{y}}\right)} \left(\frac{\langle \beta_k \rangle}{\sqrt{1-\left(\bar{\tau}_k^{\mathrm{y}}\right)^2}} - \frac{\langle \beta_k \rangle}{\bar{\tau}_k^{\mathrm{y}}} \sin^{-1}\left(\bar{\tau}_k^{\mathrm{y}}\right) - 4\left(\bar{\tau}_k^{\mathrm{y}}\right)^2 \alpha_k^2 \right), \tag{21}$$

$$\epsilon_{\text{in}}(\sigma) \approx \frac{b}{M\langle l\rangle}\begin{cases} 0, & 0 \le \sigma \le \sigma_{\text{f}}; \\ \frac{1}{8\alpha^2\left(\bar{\tau}'\right)^2}\left(2\sin^{-1}\left(\bar{\tau}'\right) - \sin\left(2\sin^{-1}\left(\bar{\tau}'\right)\right)\right), & \sigma_{\text{f}} < \sigma \le \sigma_{\text{y}}; \\ \frac{1}{8\alpha^2\left(\bar{\tau}'_{\text{y}}\right)^2}\left(2\sin^{-1}\left(\bar{\tau}'_{\text{y}}\right) - \sin\left(2\sin^{-1}\left(\bar{\tau}'_{\text{y}}\right)\right)\right) + \frac{2}{\hat{q}}\ln\left(\frac{1-\frac{\hat{q}\bar{\tau}'_{\text{y}}}{\beta}}{1-\frac{\hat{q}\bar{\tau}'}{\beta}}\right), & \sigma_{\text{y}} < \sigma < \sigma_{\text{s}}; \end{cases} , \tag{22a}$$

$$\hat{\gamma}_{\text{in}}\left(\tau/\tau_{\text{s}}\right) \equiv \frac{\gamma_{\text{in}}(\tau)}{\gamma_{\text{an}}\left(\tau_{\text{y}}\right)} = \begin{cases} \left(\frac{1-\bar{\beta}}{\hat{\tau}}\right)^2 \frac{2\sin^{-1}\left(\frac{\hat{\tau}\bar{\tau}_{\text{y}}}{1-\bar{\beta}}\right) - \sin\left(2\sin^{-1}\left(\frac{\hat{\tau}\bar{\tau}_{\text{y}}}{1-\bar{\beta}}\right)\right)}{2\sin^{-1}\left(\bar{\tau}_{\text{y}}\right) - \sin\left(2\sin^{-1}\left(\bar{\tau}_{\text{y}}\right)\right)}, & 0 < \hat{\tau} \le 1-\bar{\beta}; \\ 1 + \frac{\sin^{-1}\left(\bar{\tau}_{\text{y}}\right) - \frac{\bar{\tau}_{\text{y}}}{\sqrt{1-\bar{\tau}_{\text{y}}^2}}}{2\sin^{-1}\left(\bar{\tau}_{\text{y}}\right) - \sin\left(2\sin^{-1}\left(\bar{\tau}_{\text{y}}\right)\right)} \frac{4\bar{\beta}}{(1-\bar{\beta})}\ln\left(\frac{1-\hat{\tau}}{\bar{\beta}}\right), & 1-\bar{\beta} < \hat{\tau} < 1; \end{cases} . \tag{27}$$

Box I.

where $\hat{q}_k^{-1} \equiv \langle l_k\rangle/\langle \xi_k\rangle$ is a measure of the capacity of the dislocation network to refine the average link length, i.e. harden. Herein, the overhat $\hat{\bullet}$ indicates a given scaled variable $\bullet$.

Li and Wagoner [7] constructed a dissipative bow-out (DB) model. The increment of energy dissipated is conceptually provided by a reduction of the resolved shear stress with a static friction shear stress τ_{f}. The physical interpretation of the static friction shear stress τ_{f} is a local strengthening mechanism by various microstructural obstacles to glide, that is particularised to the experiment's materials in the following. The principle inelastic strain is as given in Box I with normalised effective resolved shear stress and yield strength,

$$\bar{\tau}' = \frac{(\sigma-\sigma_{\text{f}})}{M}\frac{\langle l\rangle}{b\mu}, \qquad \text{and} \qquad \bar{\tau}'_{\text{y}} = \frac{(\sigma_{\text{y}}-\sigma_{\text{f}})}{M}\frac{\langle l\rangle}{b\mu}, \tag{22b}$$

respectively, where $\sigma_{\text{f}} = M\tau_{\text{f}}$ is the static friction stress and σ_{s} the saturation stress. Here, α, β and $\hat{q}^{-1} = \langle l\rangle/\xi$ are the proportionality, junction formation rate and hardening ratio at the polycrystalline level. Herein, the overbar $\bar{\bullet}$ indicates a given normalised variable $\bullet$. To facilitate the subsequent numerical regression, we normalise the structural parameters in the following.

3.2. Normalisation

As plastic straining continues, the total dislocation density approaches the maximum density, $\rho \sim \rho^{\max}$, i.e. the shear flow stress asymptotically approaches the saturation shear stress

$$\tau_{\text{s}} \sim \alpha\mu b\sqrt{\rho^{\max}(\gamma)} = \frac{\beta\mu b}{\xi}. \tag{23}$$

The tangent modulus thus decreases with increasing strain, i.e. $\partial\Theta/\partial\epsilon \le 0$, which we rewrite as

$$\frac{\partial^2\tau}{\partial\gamma_{\text{in}}^2} = \frac{\tau\hat{q}^2}{4} - \frac{\beta\hat{q}}{4} \le 0. \tag{24}$$

Then the minimum mean junction formation rate becomes

$$\beta_{\min} \equiv \frac{4\alpha^2\left(\bar{\tau}_{\text{y}}\right)^3\sqrt{1-\left(\bar{\tau}_{\text{y}}\right)^2}}{\bar{\tau}_{\text{y}} - \sqrt{1-\left(\bar{\tau}_{\text{y}}\right)^2}\sin^{-1}\left(\bar{\tau}_{\text{y}}\right)}, \tag{25}$$

that is equivalent to no recovery taking place, i.e. when the average dislocation junction length at the polycrystalline level $\xi \sim 0$, and allows for scaling the junction formation rate β over the range $(0,1)$. Here, the inverted scaled mean junction formation rate $\bar{\beta} = \beta_{\min}/\beta$. The inverted scaled junction formation rate $\bar{\beta}$ thus is the measure of work-hardening capacity, where the limit zero equals perfect plasticity, and unity the absence of anelasticity and solely hardening. From here on we refer to $\bar{\beta}$ as the work-hardenability, that is unrelated to the depth to which a material is hardened after putting it through a heat treatment process [53]. Substituting the work-hardenability $\bar{\beta}$ and inverse hardening ratio $\hat{q}$ in Eq. (A.5), we define the scaled dimensionless shear stress as $\hat{\tau} \equiv \tau'/\tau_{\text{s}} = \bar{\tau}'(1-\bar{\beta})/\bar{\tau}_{\text{y}}$. This allows for scaling the normalised resolved shear stress $\hat{\tau} \in (0,1)$ as well. Hence the average dislocation segment length $\langle l\rangle$ is uniquely defined by

$$\frac{\sigma_{\text{s}}\langle l\rangle}{M\mu b}\frac{1-\bar{\beta}}{\bar{\tau}_{\text{y}}} \sim 1. \tag{26}$$

Substituting work-hardenability $\bar{\beta}$ and scaled normalised resolved shear stress $\hat{\tau}$ in Eq. (22a) and normalising the inelastic shear strain with the anelastic strain at-yield $\bar{\gamma}_{\text{an}}\left(\tau_{\text{y}}\right)$ (right-hand side of Eq. (16)), we obtain the scaled inelastic shear strain as given in Box I. Here, solely in Eq. (27) the friction stress is neglected for readability, i.e. $\sigma_{\text{f}} = 0$; in the remainder of this work, the friction stress is accounted for. Note that the constant proportionality α linearly scales the inelastic strain because it is removed by scaling with the anelastic shear strain at yield. Equations (18), (22) and (26) thus allow one to uniquely obtain the proportionality coefficient α, work-hardenability $\bar{\beta}$ and normalised yield strength $\bar{\tau}_{\text{y}}$, all at the polycrystalline level.

4. Method

In previous methodology [4–6], graphical estimates are made by means of the initial degradation of the apparent moduli [38] and a distinct transition point on the tangent modulus. Van Liempt and Sietsma [4] formulated a novel method to determine the yield stress of metals from tensile curves. The transition point is determined by a clearly distinguishable feature in a given plot of the tangent modulus versus the uniaxial normal stress. Arechabaleta et al. [5,6] propose an accessible, cheap and accurate method to quantify the dislocation network in metals, based on tensile tests and the aforementioned method [4]. A similar approach is used by Li and Wagoner [7], who closely reproduce experimental results on Dual-Phase, Transformation- and Twinning-Induced Plasticity steels. The present unified model allows us to advance this methodology, that yields the total dislocation density ρ and average segment length $\langle l\rangle$ at the polycrystalline level.

By means of the unified model, we analyse repeated cyclic uniaxial tensile tests on Interstitial-Free and Low-Alloy steels. We characterise the dislocation network evolution in relation to the macroscopic stress–strain behaviour. The present model is rooted in dislocation physics, yet general, so applicable to a wide range of metals [7]. Herein, we perform non-linear regressions on experimental force–displacement measurements. Numerical computation is limited to non-linear regression by an existing software package [54].

4.1. Experimental

Repeated cyclic tensile tests are performed on Low-Alloy (LA) and Interstitial-Free (IF) steel [6]. Both are single-phase ferritic steels. The main alloying elements for the LA steel are less than 0.08 wt% C, 0.30 wt% Mn and 0.10 wt% Si, and for the IF steel less than 0.005 wt%, 0.15 wt% Mn and 0.049 wt% Ti. Specimens of 275×10^{-3} m total length, 60×10^{-3} m gauge length and 12.5×10^{-3} m gauge width, with a thickness of 0.7×10^{-3} m are used. Note that we choose to present our results in a coherent system of units. Static loading conditions are achieved when deformation is applied slowly. The resultant static load then varies slow compared to phonon drag and thermally-activated dislocation motion [9,16].

The repeated cyclic tests consisted at most of twenty successive loading and unloading cycles with a strain rate in the order of 10^{-5} s^{-1}. In each of these cycles the stress reduces to $\sigma_f \approx 10 \times 10^6$ Pa after the application of $\Delta\epsilon_m^{pl} \approx 5 \times 10^{-3}$ true principal plastic strain. We choose to keep the friction stress constant because of the finite positive stress at load reversal. Detailed descriptions of the methodologies, specimens geometries and tensile tester is given in the works [5,6] by Arechabaleta et al.

4.2. Numerical

By means of the present method, the dislocation network structure is approximated. The present, numerical methodology is as follows (See also Fig. 4): (1) the measured force–displacement curve is transformed to the normal stress vs. principal strain curve, and the friction stress σ_f and strain σ_f/E are subtracted from the normal stress σ and the total principal strain ϵ, respectively; (2) the principal elastic strain ϵ_{el} is subtracted from total principal strain ϵ via Eq. (1), and the resolved shear stress τ and inelastic strain γ_{in} are approximated by Eq. (18); (3) the plastic hardening rate Θ_{pl} is numerically obtained by a finite-difference method, and the normalised saturation shear stress $\tau_s/(\mu b)$ is obtained by a linear fit on the plastic tangent modulus of Stage-II hardening; (4) the shear stress τ is normalised by the saturation stress τ_s, and the dislocation shear strain γ_{in} by the anelastic strain at-yield $\gamma_{an}(\tau_y)$, i.e. we obtain the scaled inelastic shear strain $\hat{\gamma}_{in}$; (5) the scaled dimensionless shear stress is multiplied by negative one, and subsequently unity is added (i.e. the scaled dimensionless shear strain–stress curve is mirrored in the vertical axis through the origin, and then shifted in the positive stress direction); and (6), the natural logarithms of the scaled shear stress, and of the scaled inelastic shear strain, i.e. $\ln(1-\tau/\tau_s)$ and $\ln(\gamma_{in}/\gamma_{an}(\tau_y))$, respectively, are calculated. A schematic representation of the steps (2–6) is given in Fig. 4.

We obtain the dependent variables α, $\bar{\beta}$ and $\bar{\tau}_y$ by a given non-linear regression with Eq. (27). Subsequently, we calculate the effective segment length $\langle l \rangle$ by means of Eq. (26) and the dislocation density as $\rho = (\alpha\langle l \rangle)^{-2}$ on the polycrystalline level. Note that the yield criterion is not restricted to our choice of strain-hardening model. However, the set of structural variables changes with the hardening models' description of dislocation network structure. The current unified model is limited to Stage-II work-hardening of a polycrystalline material. The storage and loss parameters, $\beta/\alpha b$ and ξ/b are thus obtained via Eqs. (21) and (25), respectively. However, there is not limitation to the choice of work-hardening model. For example, towards higher applied plastic strains, a phenomenological description of the complex process of Stage-III can serve a useful purpose [16].

5. Results

The loading and unloading periods are determined from the time-step vs. displacement curves, with a constant time-step period of 5×10^{-3} seconds across $> 1.8 \times 10^5$ data points. The cyclic true normal stress vs. true principal strain curves are determined from the force vs. engineering strain curves, under the assumption of a constant volume, and corrected for, by the initial engineering strain at (re)loading. The datasets of true normal stress vs. true principal strain are combined per cycle and sorted by true normal stress. The mean and the root mean square error (RMSE) are determined by a rectangular windowing function across ten neighbouring data points of equal and/or increased true normal stress. The standard deviation in true principal strain serves then as weight in the successive non-linear regressions. In Fig. 5, the cyclic true normal stress as a function of the cyclic true principal strain is given; successive cyclic results are shifted by 5×10^{-3} strain and indicated with five different, four times repeated, colours. The plastic tangent modulus is obtained by first filtering the monotonic average true normal stress vs. average true principal strain data by convolution with a block function with a width of a hundred neighbouring data points with a plastic strain range $\Delta\epsilon_{pl} \approx 10^{-6}$. Subsequently, the tangent modulus is calculated by the central-difference method. A linear regression is performed on the plastic tangent modulus, from a minimum true normal plastic stress defined with the ≤ 0.002 off-set method on the cyclic average normal stress vs. average true principal strain curves. The saturation stress σ_s is calculated by equating the Stage-II hardening model's plastic tangent modulus to zero. In Appendix B, this method is briefly summarised. The saturation stress $\sigma_s = 320 \pm 1{\times}10^6$ and $380 \pm 3{\times}10^6$ Pa for IF and LA, respectively. Here, $\pm\bullet$ indicates RMSE for independent and standard error for dependent variables. We calculate a single saturation stress σ_s for each steel grade across all loading–unloading cycles. Whereby we consider any changes in deformation conditions negligible, e.g. a changes in specimen temperature across these successive cycles. Furthermore, we find that the stress–strain range satisfies the Considère criterion [55] for uniform deformation.

The dependent variables β, α and $\bar{\tau}_y$ are obtained by first a non-linear regression on an hundredth of all data points. Herein, the non-linear regression is by the damped least-squared method [56,57]. We use a single set of material parameters, namely: elastic shear modulus $\mu = 83.8 \times 10^9$ Pa. The alloying content of IF and LA lowers the elastic modulus less than 1% of the value for pure α–Iron [58]; Poisson's ratio $\nu = 0.3$; Burgers vector magnitude $b = 2.48 \times 10^{-10}$ m [5]; and, Taylor factor $M = 3.06$ [59,60] for body-centred cubic polycrystalline material.

Because the dependent variable $\bar{\tau}_y$ lies near the edge of the permissible range $[0, 1]$, we use the natural logarithm-transformation to ensure convergence: $\bar{\tau}_y \equiv \bar{\tau}_y^{min} + \left(1 - \bar{\tau}_y^{min}\right) / \left(1 + e^{-\hat{\bar{\tau}}_y}\right)$, with the lower boundary $\bar{\tau}_y^{min} = 0.9$ and the scaled normalised yield strength $\hat{\bar{\tau}}_y \in \Re$. The latter is related to, but distinct from the normalised yield strength $\bar{\tau}_y \in (0, 1]$ and scaled dimensionless stress $\hat{\tau} \in (0, 1)$. Although dependent variable $\bar{\beta}$ shares its permissible range with $\bar{\tau}_y$, no transformation is found necessary. The initial guess for the dependent variables, informed by their geometric meaning [61], are varied across the ranges $\bar{\tau}_y \in [0.9, 0.99]$, $\alpha \in [0.1, 0.9]$ and $\bar{\beta} \in [0.1, 0.9]$, and converge to a unique set of best-fit parameters. Subsequently, the set of best-fit parameters is used to initialise the non-linear regression on the mean cyclic true normal stress vs. cyclic mean true principal strain results as presented here. The covariance matrix is determined, and the standard errors and correlation coefficients are used to calculate the standard error of the remaining physical, structural parameters, i.e. dislocation density ρ, average segment length $\langle l \rangle$ and storage rate β/α. Note that

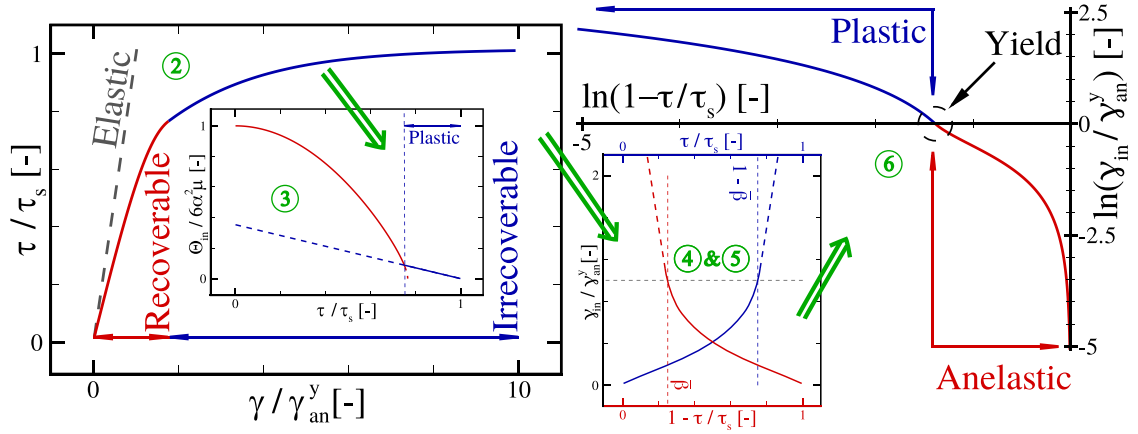

Fig. 4. Schematic representation of the present numerical methodology in steps (2–6).

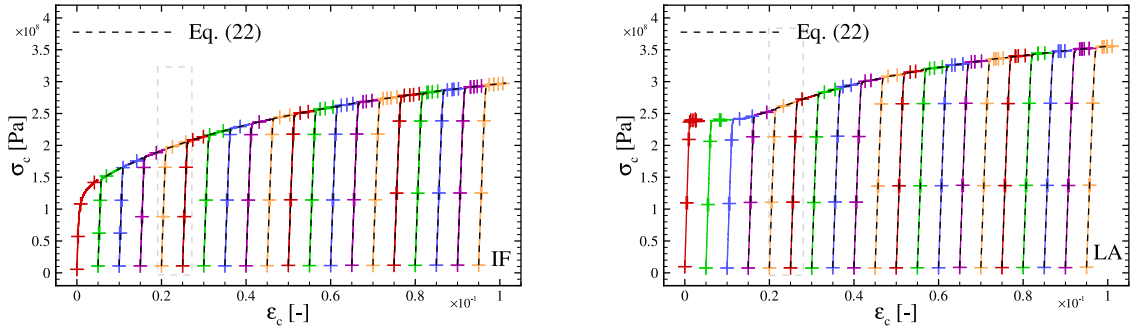

Fig. 5. The cyclic normal true stress σ_c as a function of the cyclic principal true strain ϵ_c for (a) IF and (b) LA, and the unified model prediction (22) indicated by dashed black lines. The error bars indicate the RMSEs in stress and strain per data point.

the normalised average junction length ξ/b is already uniquely defined when the saturation stress σ_s is kept constant.

The model reproductions (22) are indicated in Fig. 5 by dashed black lines. The predictions are omitted for the first loading cycle of IF and the first three of LA, due to poorness of fit and the yield point phenomenon, respectively. The former is thought to be in part due to: micro-plasticity observed in virgin materials, as discussed by Li and Wagoner [7]; internal stresses [6]; and, imperfect alignment in the samples [6]. In Fig. 6, the cyclic normal true stress σ_c as a function of the cyclic principal true strain ϵ_c, and the fit for cycle #5 are presented; the stress–strain ranges are indicated in Fig. 5 by dashed light-grey rectangles. The total cyclic inelastic strain, per cycle, is $2\times10^{-4}\cdots12\times10^{-4}$ for both steel grades. This fraction of the total cyclic inelastic strain, per cycle, increases by $1:17\cdots1:4$ and $1:10\cdots1:5$ between cycle #3 and #20, for IF and LA, respectively.

The RMSE and coefficient of determination R^2 are given in Fig. 7; the solid, coloured circles indicate the RMSE in strain over each loading cycle, and the open, coloured squares the shifted coefficient of determination $1-R^2$. The ranges of the coefficient of determination R^2 are $(0.989, 0.999)$ and $(0.994, 0.999)$ for IF and LA, respectively. In Fig. 8, the proportionality α, scaled normalised work-hardenability $\bar{\beta}/\alpha$, and yield stress σ_y and scaled normalised yield stress $\hat{\bar{\tau}}_y$ are presented; in Fig. 9, the total dislocation density ρ, the average dislocation segment length $\langle l\rangle$ and the storage rate β/α. The statistical measures and the physical parameters in Fig. 7, and Figs. 8 and 9, respectively, are

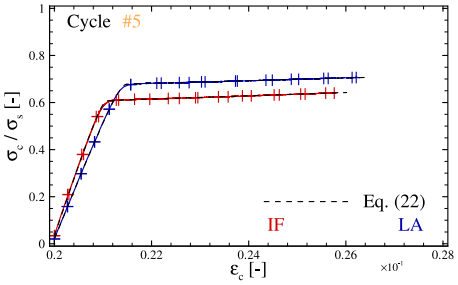

Fig. 6. The scaled cyclic normal true stress σ_c/σ_s as a function of the cyclic principal true strain ϵ_c for cycle #5 in 5(a) IF and (b) LA, and the unified model prediction (22) indicated by dashed black lines. The error bars indicate the RMSEs in stress and strain per data point.

spaced by the applied cyclic 5×10^{-3} strain so they correspond with the cyclic strains at reloading in Fig. 5.

6. Discussion

6.1. Yield strength

The Taylor relationship reads

$$\sigma_y = \sigma_0 + \alpha' M \mu b \sqrt{\rho}, \tag{28}$$

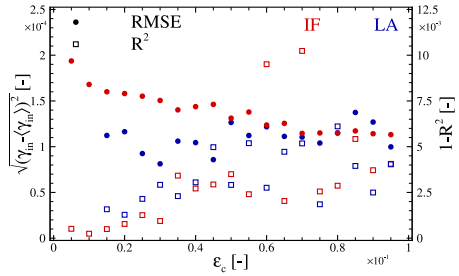

Fig. 7. The root mean-square error (RMSE) and shifted coefficient of determination $1-R^2$ as functions of the cyclic true principal strain ϵ_c for IF and LA, are indicated by coloured dots and open squares, respectively.

where $\sigma_0 \equiv M\tau_0$ is a strength contribution due to other microstructural obstacles than dislocations and α' constant. Note that Eqs. (17) and (28) differ by a factor α/α', that is not necessarily unity, because the proportionality is allowed to vary each cycle while the Taylor relationships' constant is not. Moreover, the difference between the maximum line stress σ^c (See Section 2.1) and the present observed yield strength σ_y requires explanation. It stands within reason that dislocation segments whose lengths are several times greater than the mean segment length exist [8]. Those of "*greater length*" than the average segment length are expected to control the onset of flow [26]. Considering this physical property of the dislocation network, we thus limit the present definition of the observed yield strength by

$$\sigma_y \simeq \sigma_f + M\frac{\mu b}{\langle l\rangle}. \tag{29}$$

Here, the difference between theoretical and observed yield strength is exceedingly small, but finite, due to the distributive nature of dislocation-link lengths, that comprise the given dislocation network. *It has since long been accepted that the so-called Taylor equation describes the relation between yield stress and dislocation density* [6], which warrants the validation of our hypothesis.

In Fig. 10(a), the yield stress σ_y is given as a function of the square root of the dislocation density $\sqrt{\rho}$; the dashed grey line indicates the classic Taylor relationship (i.e. $\alpha'\mu b\sqrt{\rho}$ [27]). Note that the maximum dislocation density and saturation stress are constants across loading–unloading cycles. Moreover, the maximum dislocation density ρ^{max} is defined by Eq. (23), so the scaled dislocation density ρ/ρ^{max} is independent of proportionality α.

It is clear that the classic Taylor relationship holds, with RMSEs 1.11×10^3 and 1.22×10^3 Pa, for IF and LA, respectively. Where the maximum (latter) absolute error is less than 0.1% of the saturation stress σ_s. The present definition of the observed yield strength is thus corroborated by the square root dependency of the yield stress on dislocation density. Which is testament to the success of the classic Taylor relationship [27], even though the latter is based on the force necessary for a single-character dislocation to move through a regular spaced grid of like-signed infinite straight Volterra dislocation lines. We find the physics-based local yield criterion as postulated by Gurrutxaga et al. [43], and Van Liempt and Sietsma [4], and employed by Torkabadi et al. [30] and Li and Wagoner [7].

In Fig. 10(b), the shear yield stress τ_y is presented as a function of the dislocation density ρ; the dashed coloured lines indicate the Taylor relationship (28). The origin for LA is shifted for clarity, the blue arrow indicates its original position. The constant and strength contribution $\{\alpha'\ [\text{-}], \tau_0-\tau_f\ [10^6\ \text{Pa}]\} = \{0.410, 18.7\}$ and $\{0.345, 34.0\}$; and, the RMSEs are 57×10^4 and 28×10^4 Pa for IF and LA, respectively. Standard errors are exceedingly small hence omitted here. Note that stresses σ_0 and σ_f are not necessarily equal because the former is a global strength contribution due to other microstructural obstacles than dislocations, while the latter is a local strengthening mechanism by dislocation links that "jump over" other soft pins [4,7]. Moreover, the normalised dislocation density $\rho\mu^2b^2/\sigma_s^2$ does depend on the measured proportionality α. Present definition of the observed yield strength thus is in keeping with the Taylor relationship (28) as well.

6.2. Dislocation network evolution

The statistical storage model describes the dislocation network structure evolution with plastic strain. Integrating the average segment length evolution (15) by parts and solving for the principal plastic strain, we define a scaled average dislocation segment length $\langle\hat{l}(\epsilon_{pl})\rangle \equiv \langle l(\epsilon_{pl})\rangle / \langle l(\epsilon_{pl}\to\infty)\rangle$, that decreases as:

$$\langle\hat{l}(\epsilon_{pl})\rangle = \left(\left(\langle\hat{l}(0)\rangle^{-1}-1\right)e^{-M\epsilon_{pl}\xi/(2b)}+1\right)^{-1}. \tag{30}$$

Integrating equation (19) by parts and solving for plastic strain once more, we define a scaled dislocation density $\hat{\rho}(\epsilon_{pl}) = \rho(\epsilon_{pl})/\rho(\epsilon_{pl}\to\infty)$, that increases as:

$$\hat{\rho}(\epsilon_{pl}) = \left(\left(\sqrt{\hat{\rho}(0)}-1\right)e^{-M\epsilon_{pl}\xi/(2b)}+1\right)^{2}. \tag{31}$$

Equations (30) and (31) constitute the evolution of dislocation structural parameters in the present *statistical storage model*.

We assume that physics-based structural parameters obtained at a given loading cycle are an indication of the dislocation network structure when unloading initiates in the preceding loading–unloading cycle; the dislocation network structure is preserved between unloading and subsequent reloading up to yield. Furthermore, we expect no local transformation of the dislocation structure into persistent slip bands [62] under our loading conditions [63,64]. Torkabadi et al. [30] show aforementioned assumptions to hold for Advanced High Strength Steels by comparison of monotonic and repeated cyclic uniaxial tensile test results. Hence we keep these assumptions in the remainder of the present work, which our experimental observations on the monotonic (flow) stress curves in Section 6.3 support.

In Fig. 11, the scaled dislocation density $\hat{\rho}$ is presented as a function of the monotonic plastic strain ϵ_{pl}; the scaled average dislocation segment length $\langle\hat{l}\rangle$ is given as well; the proportionality α is scaled by its number average $\langle\alpha\rangle$ over all loading–unloading cycles of a particular type of steel; and, the coloured dashed lines indicate the evolution of average dislocation segment length, dislocation density and proportionality by Eqs. (30) and (31), respectively.

In Fig. 12, the average junction length ξ is presented as a function of the monotonic plastic strain ϵ_{pl}; the physical, structural parameter ξ/b per cycle is indicated by coloured circles (See Section 5). The constant average junction lengths ξ for monotonic loading are determined as described in this section by Eq. (31), and for Stage-II hardening in Eq. (B.3). The former and latter results are indicated by solid and dashed coloured lines, respectively, and their standard errors by equivalently colour shaded areas. The average junction lengths ξ differ within 30% of each other. We argue that the origin of these differences are due to the assumption of a constant proportionality α in the present statistical storage model, and noise of the experimental signals in the first derivative of the stress–strain curves, respectively. Moreover, the storage parameter $\beta/(\alpha b)$ is presumed to be constant for Stage-II work-hardening (See Section 2.2). The storage rate β/α in Fig. 9 increases with the cyclic principal true strain ϵ_c due to the decrease in proportionality α, as shown in Figs. 11, when the junction formation rate β remains constant.

The main assumption in the statistical storage model on the dislocation structure is the constant proportionality $\alpha \equiv \left(\langle l\rangle\sqrt{\rho}\right)^{-1}$ for Stage-II work-hardening. Obviously, this holds when one combines Eqs. (30) and (31). Even so, the measured proportionality α, as displayed in Figs. 8 and 11, decreases with plastic strain. This is as rationalised by Li and Wagoner [7], who expect the proportionality α to decrease with forest dislocation density. Moreover, they [7] present an empirical linear decrease of the squared proportionality α^2 with

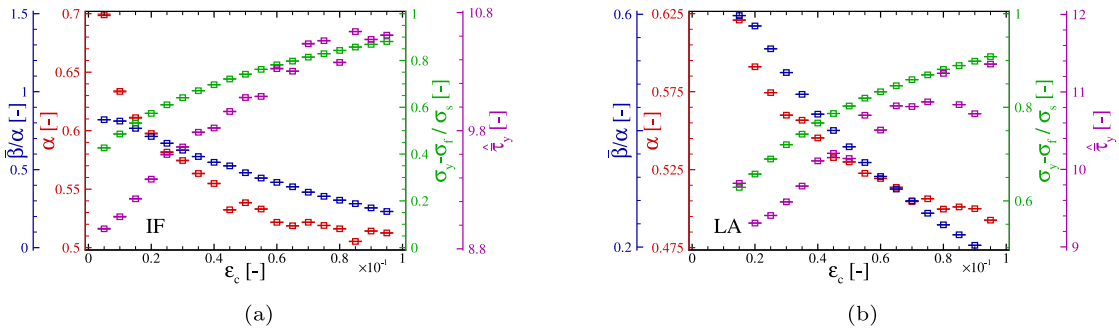

Fig. 8. The proportionality α, scaled normalised work-hardenability $\bar{\beta}/\alpha$, normalised yield stress $(\sigma_y - \sigma_f)/\sigma_s$ and scaled normalised yield stress $\hat{\bar{\tau}}_y$ as functions of the cyclic principal true strain ϵ_c for (a) IF and (b) LA. The error bars indicate the standard error in the experimentally obtained physical parameters.

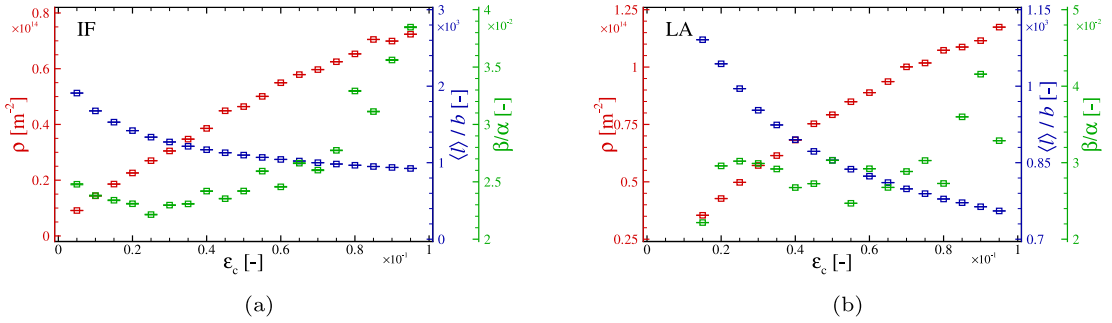

Fig. 9. The total dislocation density ρ, scaled average segment length $\langle l \rangle / b$ and storage rate β/α as functions of the cyclic principal true strain ϵ_c for (a) IF and (b) LA. The error bars indicate the standard error in the experimentally obtained physical parameters.

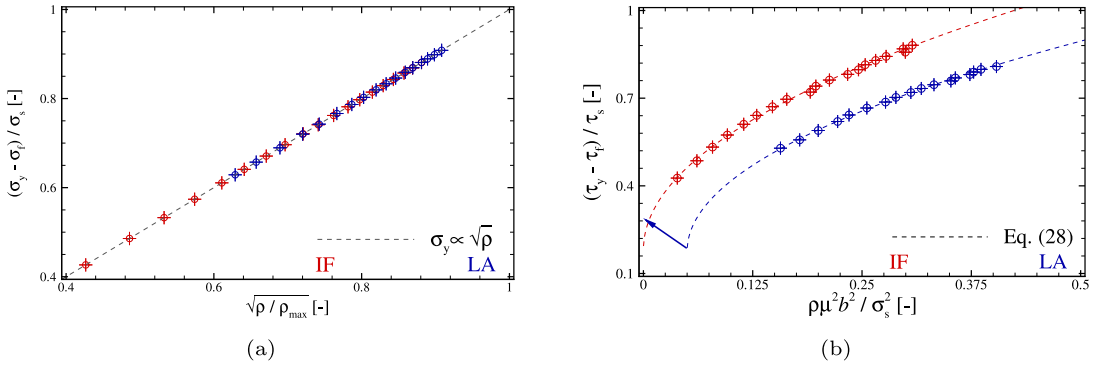

Fig. 10. (a) The scaled yield stress $(\sigma_y - \sigma_f)/\sigma_s$ as a function of the square root of the scaled dislocation density $\sqrt{\rho/\rho^{max}}$, and (b) the scaled shear flow stress $(\tau_y - \tau_f)/\tau_s$ as a function of the normalised dislocation density $\rho\mu^2 b^2/\sigma_s^2$ for IF and LA. The blue arrow indicates the original position of the origin of LA and the error bars indicate the standard error and the RMSE.

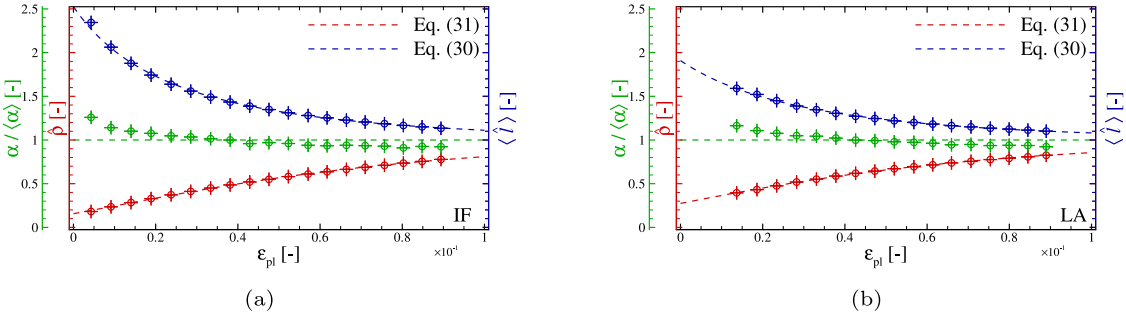

Fig. 11. The scaled dislocation density $\rho/\rho(\epsilon_{pl} \to \infty)$, scaled average dislocation segment length $\langle l \rangle / \langle l(\epsilon_{pl} \to \infty) \rangle$ and scaled proportionality $\alpha/\langle\alpha\rangle$ as functions of the monotonic plastic strain ϵ_{pl} for (a) IF and (b) LA. The error bars indicate the standard error and RMSE, and the dashed coloured lines the statistical storage model.

flow stress $\sigma \propto \sqrt{\rho}$ and expect the proportionality α to saturate with significant strain hardening. The proportionality α is obviously not constant with increasing plastic strain across the monotonic loading curve. Yet, the differences across successive loading and unloading

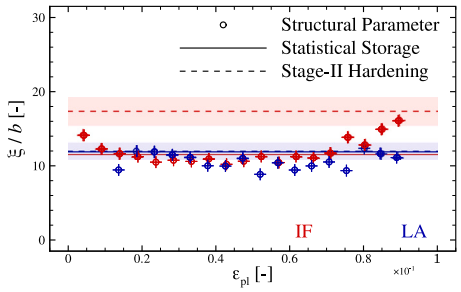

Fig. 12. The normalised average junction length ξ/b as a function of the monotonic plastic strain ϵ_{pl} for IF and LA. The error bars indicate the standard errors and RMSE, and the coloured circles the scaled junction lengths ξ/b per cycle; the solid and dashed coloured lines indicate the junction lengths ξ/b for monotonic loading, and the coloured shaded areas their standard errors.

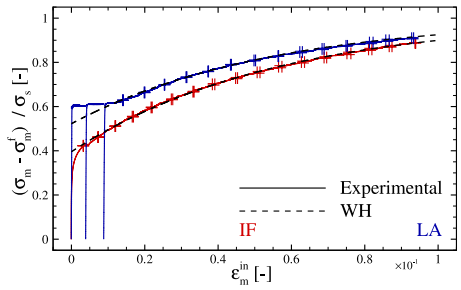

Fig. 13. The scaled, monotonic (flow) stress $\left(\sigma_{\mathrm{m}}-\sigma_{\mathrm{m}}^{\mathrm{f}}\right)/\sigma_{\mathrm{s}}$ as functions of the monotonic inelastic strain $\epsilon_{\mathrm{m}}^{\mathrm{in}}$ for IF and LA. The dashed black lines indicate the reproduction via the work-hardening (WH) model. The error bars indicate the RMSEs per data point.

cycles are tenths of their number average. So, we find that proportionality α is approximately constant and equal to $1/\left(\sqrt{\rho}\langle l\rangle\right)$ over monotonic plastic strain ranges $\epsilon_{\mathrm{pl}} \lessapprox 5\times10^{-3}$. The measured scaled mean segment length $\langle\hat{l}\rangle$ and scaled density $\hat{\rho}$ in Fig. 11 are independent of the measured proportionality α though. Moreover, the evolution of the average dislocation segment length $\langle l\rangle$ and dislocation density ρ are independent across (successive) cycles. Hence the equations (15) and (19) predict the evolution of average segment length and dislocation density for monotonic loading, which is testament to the versatility of the proto-statistical storage model [17]. However, the main assumption of the present model (See Section 1.2) is violated for monotonic loading, which we address in the following.

6.3. Work hardening

With the square root dependency of the observed yield strength (See Section 6.1) and the statistical storage model (See Section 6.2), we predict the plastic flow curve under monotonic loading. The work-hardening model is a combination of the dislocation network structural evolution (31) and the potential flow rule (17). Here we choose to describe the dislocation network by the total dislocation density alone, and use the Taylor relationship, respectively. Aforementioned combination we call the *statistical storage-based work-hardening* model.

In Fig. 13, the monotonic (flow) stress is given as a function of the monotonic inelastic strain; numerical analysis of experimental results in this section is limited to the plastic strain ranges as defined in the present work (See Sections 4 and 5); we ignore the first loading cycle of IF and first three of LA, respectively (See Section 5 as well), and the deformation pre-yield in our numerical analysis here. The dashed black lines in Fig. 13 indicate the reproduction by the statistical storage-based work-hardening (WH) model. The RMSEs across the plastic strain ranges considered in Section 5 are 1.1×10^{6} and 1.6×10^{6} for IF and LA, respectively. Equivalently, the error bars that indicate the RMSEs per data point are omitted across the stress–strain ranges that are omitted from the current numerical analysis. The monotonic flow curves are indicated by the coloured lines and globally smooth, which supports the dislocation network structure to be preserved between unloading and subsequent yield [30] (See Section 6.2).

We include in Fig. 13 the monotonic stress-monotonic inelastic strain curves of the first loading cycle of IF and the first three of LA. A given work-hardening model is obviously incapable of reproducing these stress-inelastic strain curves pre-yield, which is one of the main reasons to conduct this study. However, all experimental data is presented in Fig. 13 because they facilitate the discussion in the following.

For one, it is clear that $\sigma\propto\sqrt{\rho}$ holds during work hardening; under static loading conditions, the flow strength increase with dislocation density is captured by the Taylor relationship. Secondly, we indeed find that the (inelastic) strain in the initial cycle(s) appears to be captured by neither anelasticity nor plasticity. A potential reason is rearrangement in the dislocation network structure during the initial loading cycle [7]. For LA, the yield point elongation phenomenon is distinct; and, our method inadvertently predicts a lower yield strength [65–67]. We find that the confirmation between our model reproductions and the experimentally obtained (plastic) results for IF and LA steels notable; notable is that the reproductions indicated by dashed black lines are based on the total dislocation density ρ as measured in Section 6.2, and not obtained by regression on the experimental results as indicated by the coloured solid lines in Fig. 13. Finally, the assumption that the storage rate β/α is constant during unidirectional loading in Section 2.2 seems to hold, at least up to the first-order. Herewith we verify that the statistical storage-based WH model captures the monotonic plastic deformation. Still the functional difference between proportionality α and the Taylor relationships' constant α' requires rationalisation.

6.4. Proportionality

Recalling the Taylor relation (28), we think that the constant α' is potentially perceived as the quantitative measure between the global dislocation densities ρ and the local average dislocation segment length $\langle l\rangle$ [28], i.e. the main descriptors of dislocation network geometry. This implies that the proportionality α is an equivalent quantifier for the dislocation network geometry, and thus remains constant whilst work hardening takes place [6]. However, we find that the proportionality α decreases during plastic straining (See Section 6.2), while a large body of experimental evidence a constant $\alpha'\approx0.1\ldots0.4$ *ditto* the present work.

The success of the Taylor relation is the prediction of the flow strength increase with dislocation density whilst hardening takes place (See Section 6.3); the success of the bow-out model is the relation between global yield strength and the local dislocation structural feature of dislocation segment length [6]. As we demonstrate in Section 6.1, the Taylor relation for the shear flow strength and present definition of observed yield strength are equivalent, i.e.

$$\tau_k^{(0)}+\alpha'\mu b\sqrt{\rho\left(\gamma_k^{\mathrm{pl}}\right)}\simeq\tau_k^{\mathrm{f}}+\frac{\mu b}{\left\langle l_k\left(\gamma_k^{\mathrm{pl}}\right)\right\rangle}, \tag{32}$$

where $\tau_k^{(0)}$ is the strength contribution on slip system k other than dislocation strengthening equivalent to σ_0 in Eq. (28). When assuming the local yield and global flow strength to increase equally in strain hardening, taking the derivative with respect to the plastic strain ϵ_{pl} and using the chain rule twice, we find the ordinary differential equation

$$\frac{\partial\left\langle l\left(\epsilon_{\mathrm{pl}}\right)\right\rangle}{\partial\rho\left(\epsilon_{\mathrm{pl}}\right)}=-\frac{\alpha'\left\langle l\left(\epsilon_{\mathrm{pl}}\right)\right\rangle^{2}}{2\sqrt{\rho\left(\epsilon_{\mathrm{pl}}\right)}}. \tag{33}$$

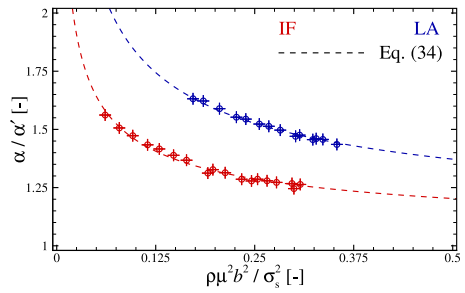

Fig. 14. The scaled proportionality α/α' as a function of the normalised dislocation density $\rho\mu^2 b^2/\sigma_s^2$ for IF and LA. The error bars indicate the standard errors; the dashed coloured lines the semi-empirical relation (34).

This is an implicit equation of the dislocation network structure evolution with plastic strain, at the polycrystalline level. We solve the ordinary differential equation (33), with the initial conditions of average dislocation segment length $\langle l\,(0)\rangle$ and dislocation density $\rho\,(0)$ at zero plastic strain, and find that the proportionality decreases as:

$$\alpha\left(\rho\left(\epsilon_{\mathrm{pl}}\right)\right) = \alpha' + \frac{\alpha(0) - \alpha'}{\sqrt{\rho\left(\epsilon_{\mathrm{pl}}\right)/\rho\,(0)}}, \tag{34}$$

with an initial proportionality $\alpha\,(0) \equiv \left(\langle l\,(0)\rangle\sqrt{\rho\,(0)}\right)^{-1}$. It is trivial that the Taylor relationship's constant $\alpha' \sim \alpha\,(\rho \to \infty)$.

In Fig. 14, the proportionality α is given as a function of the dislocation density ρ; the coloured dashed lines in Fig. 14 indicate the proportionality $\alpha\,(\rho)$, obtained by non-linear regression with Eq. (34), where the constant and initial, average dislocation segment length $\{\alpha', \langle l\,(0)\rangle/b\} = \{0.406 \pm 0.004, 4510 \pm 130\}$ and $\{0.343 \pm 0.003, 2450 \pm 30\}$ for IF and LA, respectively. Different from Arechabaleta et al. [6], and akin to Li and Wagoner ($\alpha \propto \rho^{-1/4}$) [7], we find the proportionality α has a non-linear dependence on the dislocation density ρ. The latter work [7] treats more complex microstructures beyond the present work though, e.g. various Transformation- and Twinning-Induced Plasticity Steels.

We argue that the proportionality $\alpha\,(\rho)$ is the appropriate implicit quantitative measure of the dislocation network structure evolution with plastic deformation. Coercive is the minimal difference between the constants α' obtained in Section 6.1 ($\alpha' = 0.410$ and 0.345 for IF and LA, respectively) and the current section, which are obtained independently. Moreover, the RMSEs are 4.4×10^{-3} and 2.1×10^{-3}, for IF and LA, respectively, and the shifted coefficient of determination $1 - \mathrm{R}^2 < 10^{-4}$. The minimum proportionality $\alpha\left(\gamma_{\mathrm{pl}}\right) \sim \alpha'$ is obviously only achieved when dislocation recovery or rearrangement processes are absent. The constant α' thus is a lower limit of the quantitative representation of the dislocation network geometry α, i.e. a physics-based, yet theoretical, asymptote. We issue a warning to the reader here on the physical interpretation of constant α'. It seems tempting to relate the constant α' directly with the forest strengthening [7], as the projection of dislocation links that intersect a given glide plane is constant. Detractive is the change in constant α' with steel type though, which can be remedied by changing the elastic shear modulus. However, use of the Taylor factor to relate principal inelastic strain and normal stress to local inelastic shear strain and shear stress, convolutes any such interpretation. Furthermore, the proportionality α in Eq. (22) is an effective measure at the polycrystalline level, that neglects the notion of active and inactive slip-systems. The success of Eq. (34) combined with the present statistical storage model, excludes the seminal interpretation of the Taylor relationships' constant α' as the measure of dislocation–dislocation interaction on a single slip-system though. Hence we interpret the Taylor relationship as a combination of forest interactions and junction strengthening, akin to Kubin et al. [29]. Here, the proportionality α thus is the effective measure of junction strengthening on the crystallite level (See Section 2.2), that changes with plastic strain through forest interactions [7].

Equation (32) remains an *a posteriori* constructed semi-empirical relation, that is based solely on the interpretation of the experimental results with our present model (i.e. with a constant proportionality α per loading–unloading cycle). Use of the ordinary differential equation (33) in the present statistical storage model, in Section 2.2, will enforce the equivalence in Eq. (32). Then, the interpretation of the constant α' is set *a priori*, which we think severely weakens the results herein. The current work thus presents the next step [6] towards the final interpretation of the Taylor relationship.

In the present model, we consider solely monotonous, unidirectional loading wherefore the current modelling framework, as the works [4–7] show, is adequate. For pre-yield tension–compression asymmetry Zhu et al. [33] recently present a combined experimental-modelling approach. We do not account for strain gradients or internal stresses, which are postulated as critical in understanding anelasticity under reciprocal loading conditions [7]. Full-Field crystal plasticity methods are the only way to satisfy mechanical equilibrium and strain compatibility throughout a polycrystal. Hence they will give more realistic results than our Taylor homogenisation, e.g. the influence of the accumulation of dislocations at grain boundaries, which we do not capture in this model (See Section 3). However, the present experimental data leads to over-fitting when one employs a more sophisticated full-field crystal plasticity method. Our framework is accepted in inelastic deformation modelling, and demonstrates its usefulness in anelasticity by e.g. Li and Wagoner [7] and plasticity by e.g. Sendrowic et al. [68] to date. In the following, we summarise several universal, experimental observations that support our findings.

6.5. Apparent modulus

Given that the elastic modulus is virtually constant with strain, the degradation in apparent modulus is primarily due to anelastic deformation [1]. With successive loading–unloading cycles the dislocation density ρ increases and the average segment length $\langle l\rangle$ decreases (See Section 6.2). The associated change in dislocation network is such that the product $b\rho\langle l\rangle$ (See Eq. (6)), i.e. the anelastic strain magnitude, increases with each loading–unloading cycle (See Section 5). For a given applied uniaxial, cyclic tension, σ_c, well below the yield strength σ_y, the anelastic modulus thus decreases, i.e. the apparent modulus degradates.

Ma et al. [35] present a series of continuous loading–unloading–reloading experiments on a near-alpha high-strength titanium alloy within the cold and warm forming domains. They [35] find that the chord modulus under cold deformation is degraded dramatically at a low plastic strain level and then gradually gets a saturated state with dislocation density. Chamakura et al. [42] experimentally observe independent of the unified model herein that the modified chord modulus, which is proportional to the chord modulus but can be an order of magnitude higher, decreases with dislocation density in cyclic loading–unloading tensile tests on fully martensitic stainless steel. Most recently, Vitzthum et al. [32] presents continuous cyclic tensile test on a DP and IF steel, that are similar to those herein. They [32] observe that the loading and unloading chord moduli decrease with increasing plastic strain, where in the beginning of plastic deformation, these moduli decrease rapidly until they converge with further plastic deformation.

The initial anelastic modulus reads $\Theta_{\mathrm{an}} \propto \alpha^2$. Hence the now known proportionality evolution, $\alpha\,(\rho)$, allows us to rationalise the following observations: *one*, the variation of the apparent modulus depends on prior plastic straining [32,35,40–42]; *two*, the apparent modulus decreases to a certain extent, and then saturates with work hardening, i.e. successive plastic deformation does not lead to an experimentally observable decrease in modulus [32,35,40]; *three*, (recovery) heat treatment increases/restores the apparent modulus [35,39]; and

four, the apparent modulus approaches the theoretical elastic modulus after bake-hardening [30], while the flow strength is unaffected, i.e. the dislocation density is virtually constant.

We find that: *one*, with work hardening and ensuing plastic deformation the proportionality decreases with dislocation density; *two*, because of the recovery and/or rearrangement process in Stage-II strain-hardening, the dislocation density saturates, similarly the change of initial anelastic modulus with plastic strain does. Alike our findings (not presented in this work), Vitzthum et al. [32] find the loading modulus for single-phase material decreases less with increasing plastic strain then the loading modulus of Dual-Phase steel; *three*, heat treatment reduces the dislocation density by increased dislocation recovery, which leads to a higher apparent modulus. This is inline with the extensive experimental results on warm deformation by Ma et al. [35]. They [35] show that the modulus degradation and its strain dependence decrease with forming temperature; and *four*, interstitials diffuse to dislocation lines, so the average dislocation segment lengths decrease with bake-hardening, yet dislocation recovery is minimal, so the proportionality α increases. For the influences of metals lattices, local dislocation network structure and compressibility, we refer to our previous work on the influence of dislocations on the apparent elastic constants in single metallic crystallites [31,33].

To accurately predict the apparent modulus (i.e the anelastic strain) after plastic deformation, one needs a dislocation network structure model which *a priori* incorporates the evolution of proportionality $\alpha\left(\epsilon_{\mathrm{pl}}\right)$. The relationship given by Eq. (33) is not enforced in the current statistical storage-based WH model though. However, future storage models are to be amended with the now known dependence of the proportionality α on the dislocation density ρ.

7. Conclusions

We present a static inelastic model. The elastic mechanical behaviour is described by isotropic linear elasticity, anelastic mechanical behaviour by the dissipative dislocation bow-out model and the dislocation network structure evolution by the statistical storage model. We analyse repeated cyclic tensile tests on Interstitial-Free and Low-Alloy steels. The yield point is determined by the compliance of anelastic and plastic deformation. We ascertain the two premises in physical metallurgy of the Taylor relationship and the statistical storage-based work-hardening. Finally, we present a measure for the changes in initial apparent modulus with thermomechanical processing.

Under the assumption that the dislocation network structure is preserved between unloading from the plastic regime and subsequent reloading up to yield, we draw the following conclusions: the statistical storage model predicts the evolution of average segment length and dislocation density with plastic strain; and, the statistical storage-based work-hardening model is experimentally verified, and successfully predicts monotonic uniaxial plastic deformation at least up to the first-order. Herein, we experimentally verify that the flow strength is predicted by Taylor-type equations.

In this work, fundamental understanding on the evolution of dislocation network geometry during plastic deformation is expanded as well. The implicit semi-empirical relation of the proportionality, $\alpha\left(\rho\right) \propto 1/\sqrt{\rho}$, captures the average dislocation segment length decrease and dislocation density increase with work hardening, i.e. the chance in dislocation network structure. We thus refine the physical interpretation of the constant α' in the Taylor relationship to the theoretical asymptotic lower limit of the dislocation network geometry. Moreover, we interpret the Taylor relationship as a combination of forest interactions and junction strengthening. The now known evolution of the proportionality between average segment length and dislocation density allows for statistical work-hardening models to be further improved.

Summarising, we expand understanding on the fundamental relationships between the plastic deformation and the dislocation network structure, and mechanical properties of anelasticity, yield and flow. One ulterior application of present, novel interpretation of yield and the unified model is to predict inelastic deformation by means of full-field crystal plasticity modelling [69].

Declaration of competing interest

The authors declare that they have no known competing financial interests or personal relationships that could have appeared to influence the work reported in this paper.

Acknowledgements

This research was carried out under project number T17019n in the framework of the Research Program of the Materials innovation institute (M2i) (www.m2i.nl) supported by the Dutch government. The authors acknowledge the kind contribution by Zaloa Arechabaleta of making the experimental data available.

Appendix A. Inelastic shear

The normalised anelastic shear strain is

$$\bar{\gamma}_k^{\mathrm{an}}\left(\bar{\tau}\right) \equiv \gamma_k^{\mathrm{an}} \frac{\langle l_k \rangle}{b} = \frac{1}{8\alpha_k^2 \left(\bar{\tau}_k\right)^2} \left(2\sin^{-1}\left(\bar{\tau}_k\right) - \sin\left(2\sin^{-1}\left(\bar{\tau}_k\right)\right)\right), \tag{A.1}$$

where the normalised shear stress is

$$\bar{\tau}_k \equiv \frac{\tau_k}{\tau_k^{\mathrm{c}}} = \frac{\tau_k \langle l_k \rangle}{b\mu}, \tag{A.2}$$

with the maximum line stress $\tau_k^{\mathrm{c}} \equiv b\mu/\langle l_k \rangle$. The normalised anelastic tangent modulus is

$$\frac{\Theta_k^{\mathrm{an}}}{\mu} \equiv \left(\frac{\partial \bar{\gamma}_k^{\mathrm{an}}}{\partial \bar{\tau}_k}\right)^{-1} = \frac{2\alpha_k^2 \left(\bar{\tau}_k\right)^2}{\frac{1}{\sqrt{1-\left(\bar{\tau}_k\right)^2}} - \frac{1}{\bar{\tau}_k}\sin^{-1}\left(\bar{\tau}_k\right)}. \tag{A.3}$$

Equation (19) is a separable differential equation for the plastic shear strain:

$$\int_{\gamma_k^{\mathrm{pl}}\left(\tau_k^{\mathrm{y}}\right)}^{\gamma_k^{\mathrm{pl}}(\tau_k)} \mathrm{d}\gamma' = \int_{\rho_k\left(\tau_k^{\mathrm{y}}\right)}^{\rho_k(\tau_k)} \left(\frac{\langle \beta_k \rangle}{\alpha_k b}\sqrt{\rho'} - \frac{\langle \xi_k \rangle}{b}\rho'\right)^{-1} \mathrm{d}\rho', \tag{A.4}$$

where $\tau_k^{\mathrm{y}} \leq \tau_k^{\mathrm{c}}$ is the yield strength. The normalised plastic shear strain for a finite shear stress is

$$\bar{\gamma}_k^{\mathrm{pl}} = \frac{2}{\hat{q}_k} \ln\left(\left(1 - \frac{\hat{q}_k \bar{\tau}_k^{\mathrm{y}}}{\langle \beta_k \rangle}\right) / \left(1 - \frac{\hat{q}_k \bar{\tau}_k}{\langle \beta_k \rangle}\right)\right), \tag{A.5}$$

with a dimensionless parameter $\hat{q}_k \equiv \langle \xi_k \rangle / \langle l_k \rangle$ that is detailed in Section 3.1. The normalised hardening modulus is

$$\frac{\Theta_k^{\mathrm{pl}}}{\mu} \equiv \left(\frac{\partial \bar{\gamma}_k^{\mathrm{pl}}}{\partial \bar{\tau}_k}\right)^{-1} = \frac{\langle \beta_k \rangle}{2}\left(1 - \frac{\hat{q}_k \bar{\tau}_k}{\langle \beta_k \rangle}\right). \tag{A.6}$$

Appendix B. Stage-II work-hardening

The majority of stage-II work-hardening models have the form:

$$\frac{\partial \rho}{\partial \epsilon_{\mathrm{pl}}} \approx C_1 \sqrt{\rho\left(\epsilon_{\mathrm{pl}}\right)} - C_2 \rho\left(\epsilon_{\mathrm{pl}}\right), \tag{B.1}$$

where C_1 and C_2 are constants with units m^{-1} and no dimension, respectively. Equation (B.1) describes the development of the dislocation density as a function of the true plastic principal strain ϵ_{pl}. Note that glide plane and slip system remain unspecified here, and the dislocation properties are omitted for clarity; the type of dislocation density varies between theories. Equation (B.1) is identical in form to Vetter's version of Bergström's equation, that considers the immobile dislocation density alone [70,71], and the proto-statistical storage model by Kocks (See

Section 2.2), that originally treats forest dislocations [10]. Combining the (classic) Taylor relationship for the flow strength, $\sigma \sim \alpha' M \mu b \sqrt{\rho}$, and Eq. (B.1), one obtains the plastic tangent modulus

$$\Theta_{\mathrm{pl}}\left(\epsilon_{\mathrm{pl}}\right) \approx \frac{1}{2}\alpha' C_1 M \mu b - \frac{1}{2} C_2 \sigma\left(\epsilon_{\mathrm{pl}}\right). \tag{B.2}$$

The saturation stress σ_{s} thus is

$$\sigma_{\mathrm{s}} \equiv \lim_{\epsilon_{\mathrm{pl}} \to \infty} \sigma\left(\epsilon_{\mathrm{pl}}\right) \sim \frac{\alpha' C_1 M \mu b}{C_2}. \tag{B.3}$$

Rewriting Eq. (19) as a function of the true plastic principal strain ϵ_{pl}, and comparing the result with Eqs. (B.2), we find

$$\beta \approx \frac{\alpha' C_1 b}{M}; \quad \text{and,} \quad \xi \approx \frac{C_2 b}{M}, \tag{B.4}$$

where ξ is the effective junction length. Equation (B.3) is then used to determine the saturation stress σ_{s} by linear regression on the plastic tangent modulus, and Eq. (B.4) for comparison with the here summarised seminal approach.

References

[1] J.D. Eshelby, Dislocations as a cause of mechanical damping in metals, Proc. R. Soc. Lond. Ser A 197 (1050) (1949) 396–416.
[2] J. Koehler, G. DeWit, Influence of elastic anisotropy on the dislocation contribution to the elastic constants, Phys. Rev. 116 (5) (1959) 1121.
[3] B.K. Agrawal, G. Verma, Dislocation contribution to the elastic constants of body-centered cubic crystals, Phys. Rev. 127 (2) (1962) 501.
[4] P. van Liempt, J. Sietsma, A physically based yield criterion I. Determination of the yield stress based on analysis of pre-yield dislocation behaviour, Mater. Sci. Eng. A 662 (2016) 80–87.
[5] Z. Arechabaleta, P. van Liempt, J. Sietsma, Quantification of dislocation structures from anelastic deformation behaviour, Acta Mater. 115 (2016) 314–323.
[6] Z. Arechabaleta, P. van Liempt, J. Sietsma, Unravelling dislocation networks in metals, Mater. Sci. Eng. A 710 (2018) 329–333.
[7] D. Li, R. Wagoner, The nature of yielding and anelasticity in metals, Acta Mater. (2020) 116625.
[8] R.B. Sills, N. Bertin, A. Aghaei, W. Cai, Dislocation networks and the microstructural origin of strain hardening, Phys. Rev. Lett. 121 (8) (2018) 085501.
[9] D. Hull, D.J. Bacon, Introduction to Dislocations, Vol. 37, Elsevier, 2011.
[10] D. Kuhlmann-Wilsdorf, Questions you always wanted (or should have wanted) to ask about work-hardening, Mater. Res. Innov. 1 (4) (1998) 265–297.
[11] D. Kuhlmann-Wilsdorf, LEDS: Properties and effects of low energy dislocation structures, Mater. Sci. Eng. 86 (1987) 53–66.
[12] A. Cottrell, The properties of materials at high rates of strain, in: London Conference of Institute of Mechanical Engineers, IME, London, 1957, 1957, p. 18.
[13] K. Srivastava, D. Weygand, D. Caillard, P. Gumbsch, Repulsion leads to coupled dislocation motion and extended work hardening in BCC metals, Nature Commun. 11 (1) (2020) 1–8.
[14] F. Frank, W. Read Jr., Multiplication processes for slow moving dislocations, Phys. Rev. 79 (4) (1950) 722.
[15] F.C. Frank, The Frank–Read source, Proc. R. Soc. Lond. Ser. A Math. Phys. Eng. Sci. 371 (1744) (1980) 136–138.
[16] P.M. Anderson, J.P. Hirth, J. Lothe, Theory of Dislocations, Cambridge University Press, 2017.
[17] U. Kocks, Laws for work-hardening and low-temperature creep, J. Eng. Mater. Technol. 98 (1) (1976) 76–85.
[18] U. Kocks, H. Mecking, Physics and phenomenology of strain hardening: The FCC case, Prog. Mater. Sci. 48 (3) (2003) 171–273.
[19] Y. Estrin, H. Mecking, A unified phenomenological description of work hardening and creep based on one-parameter models, Acta Metall. 32 (1) (1984) 57–70.
[20] Y. Bergström, W. Roberts, A dislocation model for dynamical strain ageing of α-iron in the jerky-flow region, Acta Metall. 19 (11) (1971) 1243–1251.
[21] Y. Bergström, H. Hallén, An improved dislocation model for the stress-strain behaviour of polycrystalline α-Fe, Mater. Sci. Eng. 55 (1) (1982) 49–61.
[22] P. Van Liempt, Workhardening and substructural geometry of metals, J. Mater Process. Technol. 45 (1–4) (1994) 459–464.
[23] P. Van Liempt, M. Onink, A. Bodin, Modelling the influence of dynamic strain ageing on deformation behaviour, Adv. Eng. Mater. 4 (4) (2002) 225–232.
[24] F. Roters, D. Raabe, G. Gottstein, Work hardening in heterogeneous alloys-a microstructural approach based on three internal state variables, Acta Mater. 48 (17) (2000) 4181–4189.
[25] A. Ma, F. Roters, A constitutive model for FCC single crystals based on dislocation densities and its application to uniaxial compression of aluminium single crystals, Acta Mater. 52 (12) (2004) 3603–3612.
[26] S. Akhondzadeh, R.B. Sills, N. Bertin, W. Cai, Dislocation density-based plasticity model from massive discrete dislocation dynamics database, J. Mech. Phys. Solids (2020) 104–152.
[27] G.I. Taylor, The mechanism of plastic deformation of crystals. Part I.—Theoretical, Proc. R. Soc. Lond. Ser. A Math. Phys. Eng. Sci. 145 (855) (1934) 362–387.
[28] G. Saada, Sur le durcissement dû à la recombinaison des dislocations, Acta Metall. 8 (12) (1960) 841–847.
[29] L. Kubin, B. Devincre, T. Hoc, Toward a physical model for strain hardening in FCC crystals, Mater. Sci. Eng. A 483 (2008) 19–24.
[30] A. Torkabadi, E. Perdahcıoğlu, V. Meinders, A. van den Boogaard, On the nonlinear anelastic behavior of AHSS, Int. J. Solids Struct. 151 (2018) 2–8.
[31] J.S. Van Dokkum, C. Bos, S.E. Offerman, J. Sietsma, Influence of dislocations on the apparent elastic constants in single metallic crystallites: An analytical approach, Materialia 20 (2021) 101178.
[32] S. Vitzthum, J.R. Kornmeier, M. Hofmann, M. Gruber, R. Norz, E. Maawad, J. Mendiguren, W. Volk, In-situ analysis of the elastic-plastic characteristics of high strength dual-phase steel, Mater. Sci. Eng. A (2022) 144097.
[33] G. Zhu, C. Yang, G. Shen, Y. Peng, B. Shi, The asymmetric pre-yielding behaviour during tension and compression for a rolled AZ31 Mg alloy, Int. J. Mater. Form. 15 (3) (2022) 1–12.
[34] J. Ma, H. Li, M. Fu, Modelling of springback in tube bending: A generalized analytical approach, Int. J. Mech. Sci. 204 (2021) 106516.
[35] J. Ma, H. Li, Z. He, H. Yang, M. Fu, Complex unloading behavior of titanium alloy in cold and thermal-mechanical working, Int. J. Mech. Sci. 233 (2022) 107672.
[36] H. Mecking, U. Kocks, Kinetics of flow and strain-hardening, Acta Metall. 29 (11) (1981) 1865–1875.
[37] A. Benzerga, Y. Bréchet, A. Needleman, E. Van der Giessen, Incorporating three-dimensional mechanisms into two-dimensional dislocation dynamics, Modelling Simul. Mater. Sci. Eng. 12 (1) (2003) 159.
[38] G. Schoeck, Dislocation theory of plasticity of metals, in: Advances in Applied Mechanics, Vol. 4, Elsevier, 1956, pp. 229–279.
[39] K. Yamaguchi, H. Adachi, N. Takakura, Effects of plastic strain and strain path on Youngs modulus of sheet metals, Met. Mater. 4 (3) (1998) 420–425.
[40] J. Benito, J. Jorba, J. Manero, A. Roca, Change of Young's modulus of cold-deformed pure iron in a tensile test, Metall. Mater. Trans. A 36 (12) (2005) 3317–3324.
[41] R. Perez, J. Benito, J. Prado, Study of the inelastic response of TRIP steels after plastic deformation, Isij Int. 45 (12) (2005) 1925–1933.
[42] J. Chamakura, A. Riemslag, T. Reinton, V. Popovich, J. Sietsma, The quantitative relationship between non-linear stress-strain behaviour and dislocation structure in martensitic stainless steel, Acta Mater. 240 (2022) 118364.
[43] B. Gurrutxaga-Lerma, D. Balint, D. Dini, A. Sutton, The mechanisms governing the activation of dislocation sources in aluminum at different strain rates, J. Mech. Phys. Solids 84 (2015) 273–292.
[44] Y. Estrin, Dislocation-density-related constitutive modeling, in: Unified Constitutive Laws of Plastic Deformation, Vol. 1, Academic, San Diego, CA, 1996, pp. 69–106.
[45] E. Voce, The relationship between stress and strain for homogeneous deformation, J. Inst. Met. 74 (1948) 537–562.
[46] J. Palm, Stress-strain relations for uniaxial loading, Flow Turbul. Combust. 1 (1) (1949) 198.
[47] D. Kuhlmann-Wilsdorf, Unified Theory of Stages II and III of Workhardening in Pure FCC Metal Crystals, Tech. Rep., Virginia Univ., Charlottesville. School of Engineering and Applied Science, 1966.
[48] U. Kocks, A. Argon, M. Ashby, Thermodynamics and kinetics of slip, 1975, Prog. Mater. Sci. 19.
[49] E. Nes, Modelling of work hardening and stress saturation in FCC metals, Prog. Mater. Sci. 41 (3) (1997) 129–193.
[50] E. Nes, K. Marthinsen, B. Holmedal, The effect of boundary spacing on substructure strengthening, Mater. Sci. Technol. 20 (11) (2004) 1377–1382.
[51] E. Demir, A physically based constitutive model for FCC single crystals with a single state variable per slip system, Modelling Simul. Mater. Sci. Eng. 25 (1) (2016) 015009.
[52] R. Madec, B. Devincre, L. Kubin, T. Hoc, D. Rodney, The role of collinear interaction in dislocation-induced hardening, Science 301 (5641) (2003) 1879–1882.
[53] W. Jominy, A. Boegehold, A hardenability test for carburizing steel, Trans. ASM 26 (1938) 574–606.
[54] I. Wolfram Research, Mathematica, version 13.1, 2022, Champaign, IL.
[55] A. Considère, Annales des ponts et chaussées, I Sem. 574 (1885).
[56] K. Levenberg, A method for the solution of certain non-linear problems in least squares, Quart. Appl. Math. 2 (2) (1944) 164–168.
[57] D.W. Marquardt, An algorithm for least-squares estimation of nonlinear parameters, J. Soc. Ind. Appl. Math. 11 (2) (1963) 431–441.
[58] G. Ghosh, G. Olson, The isotropic shear modulus of multicomponent Fe-base solid solutions, Acta Mater. 50 (10) (2002) 2655–2675.
[59] J. Rosenberg, H. Piehler, Calculation of the Taylor factor and lattice rotations for BCC metals deforming by pencil glide, Metall. Trans. 2 (1) (1971) 257–259.

[60] R. Stoller, S. Zinkle, On the relationship between uniaxial yield strength and resolved shear stress in polycrystalline materials, J. Nucl. Mater. 283 (2000) 349–352.
[61] H.J. Berendsen, A Student's Guide to Data and Error Analysis, Cambridge University Press, 2011.
[62] J. Friedel, The mechanism of work-hardening and slip-band formation, Proc. R. Soc. Lond. Ser. A. 242 (1229) (1957) 147–159.
[63] P. Lukáš, L. Kunz, Role of persistent slip bands in fatigue, Phil. Mag. 84 (3–5) (2004) 317–330.
[64] S.K. Paul, A critical review of experimental aspects in ratcheting fatigue: Microstructure to specimen to component, J. Mater. Res. Technol. 8 (5) (2019) 4894–4914.
[65] R. Schwab, V. Ruff, On the nature of the yield point phenomenon, Acta Mater. 61 (5) (2013) 1798–1808.
[66] R. Schwab, Understanding the complete loss of uniform plastic deformation of some ultrafine-grained metallic materials in tensile straining, Int. J. Plast. 113 (2019) 218–235.
[67] R. Schwab, A. Harter, Extracting true stresses and strains from nominal stresses and strains in tensile testing, Strain 57 (6) (2021) e12396.
[68] A. Sendrowicz, A. Myhre, I. Yasnikov, A. Vinogradov, Stored and dissipated energy of plastic deformation revisited from the viewpoint of dislocation kinetics modelling approach, Acta Mater. (2022) 118190.
[69] F. Roters, M. Diehl, P. Shanthraj, P. Eisenlohr, C. Reuber, S.L. Wong, T. Maiti, A. Ebrahimi, T. Hochrainer, H.-O. Fabritius, et al., DAMASK–The Düsseldorf advanced material simulation kit for modeling multi-physics crystal plasticity, thermal, and damage phenomena from the single crystal up to the component scale, Comput. Mater. Sci. 158 (2019) 420–478.
[70] R. Vetter, A. Van Den Beukel, Dislocation production in cold worked copper, Scr. Metall. 11 (2) (1977) 143–146.
[71] P. van Liempt, Yield and Flow Stress of Steel in the Austenitic State (Ph.D. thesis), Delft University of Technology, 2016.